A Data-Based Artificial Neural Network Assisted Testing Framework for the Assessment of Electrical Stimulation Patterns for Retinal Implants

Dissertation

der Mathematisch-Naturwissenschaftlichen Fakultät

der Eberhard Karls Universität Tübingen

zur Erlangung des Grades eines

Doktors der Naturwissenschaften

(Dr. rer. nat.)

vorgelegt von

Achim Speck

aus Engen

Tübingen

2019

Gedruckt mit Genehmigung der Mathematisch-Naturwissenschaftlichen Fakultät der Eberhard Karls Universität Tübingen.

Tag der mündlichen Qualifikation:	12.03.2020
Dekan:	Prof. Dr. Wolfgang Rosenstiel
1. Berichterstatter:	Prof. Dr. Eberhart Zrenner
2. Berichterstatter:	Prof. Dr. Hanspeter Mallot

For my family.

Contents

1 Introduction **1**

1.1 The Vertebrate Eye & the Retina 2

1.1.1 The Eye 2

1.1.2 The Retina 3

1.2 Electrical Retinal Implants 6

1.3 Motivation 8

1.3.1 Objectives & Approach 10

2 Methods **12**

2.1 Electro-Physiological Experimental Set-Up 13

2.2 Multielectrode Stimulation & Recordings 15

2.2.1 Animal Tissues 15

2.2.2 Tissue Sample Preparation 15

2.2.3 Recording Procedure 16

2.2.4 Stimulation Patterns 16

Light Stimulation 16

Electrical Stimulation 19

2.3 Data Processing 20

2.4 Artificial Neural Network based Object Discrimination 22

2.4.1 Artificial Neural Network Architecture & Training 22

Pre-Evaluation of Light Stimulation induced Responses . . . 22

Convolutional Neural Network based Analysis 24

3 Results **28**

3.1 Stimulus-Dependent Retinal Ganglion Cell Responses 29

3.1.1 Responses to Light Flash Stimulation 29

3.1.2 Spatial Spread & Time Course of Responses 31

3.1.3 Direction Selective Activity 37

3.1.4 Stimulus Anticipation indicated by Retinal Ganglion Cell Responses 38

3.2 Assessment of Electrically induced Retinal Ganglion Cell Responses 41

Light Stimulation induced Response Library for Training . . 41

Electrical Stimulation induced Response Library for Testing 42

3.2.1 Artificial Neural Network based Pre-Evaluation of Light Stimulation induced Responses 43

3.2.2 Classification with Convolutional Neural Networks 45

3.2.3 Electrical Stimulation Patterns for the Application in Retinal Implants 52

4 Discussion & Conclusions **55**

4.1 Retinal Ganglion Cell Responses 56

4.1.1 Spatial & Temporal Properties of Retinal Ganglion Cell Responses 56

4.1.2 Independence of Stimulus Direction 58

4.1.3 Retinal Stimulus Anticipation 59

4.2 Object Discrimination 60

4.2.1 Classification of Retinal Ganglion Cell Response Patterns . . 60

4.2.2 Light Stimulation Patterns for Reference Data 63

4.2.3 Plausibility of the Data-Based Artificial Neural Network Assisted Testing Approach 64

4.2.4 Modifications & Extensions of the Framework 66

4.2.5 Implications for the Development of Electrical Retinal Implants 67

4.3 Conclusion 69

5 Summary **70**

6 Zusammenfassung **71**

7 Abbreviations **72**

8 Bibliography **73**

9 List of Figures **87**

10 Acknowledgements **90**

Chapter 1

Introduction

This first chapter introduces the vertebrate eye and the retina on a mainly functional level, which includes a brief explanation of retinal cell types and retinal feature detection mechanisms. Further, the restoration of visual perception to blind patients through the application of electrical stimulation using retinal prostheses is explained. The final section describes the motivation of this study and explains the objectives and the general approach.

1.1 The Vertebrate Eye & the Retina

1.1.1 The Eye

Vertebrates' eyes have a common structural layout. A flexible and robust tissue, the sclera, forms the outer layer of an eyeball. The vascular layer beneath is called the choroid and is responsible for blood supply through its' vessels, to nourish the retina. The transparent vitreous body has a gelatinous morphology and embodies the physically biggest part of the eye. The pupil can be thought of as the pinhole in a camera and is located in front of the lens. Light enters the eye through the pupil and is then focused onto the retina by the cornea and the lens (Rodieck, 1998). Figure 1.1 shows a schematic representation of the sagittal section of the eye and the retina.

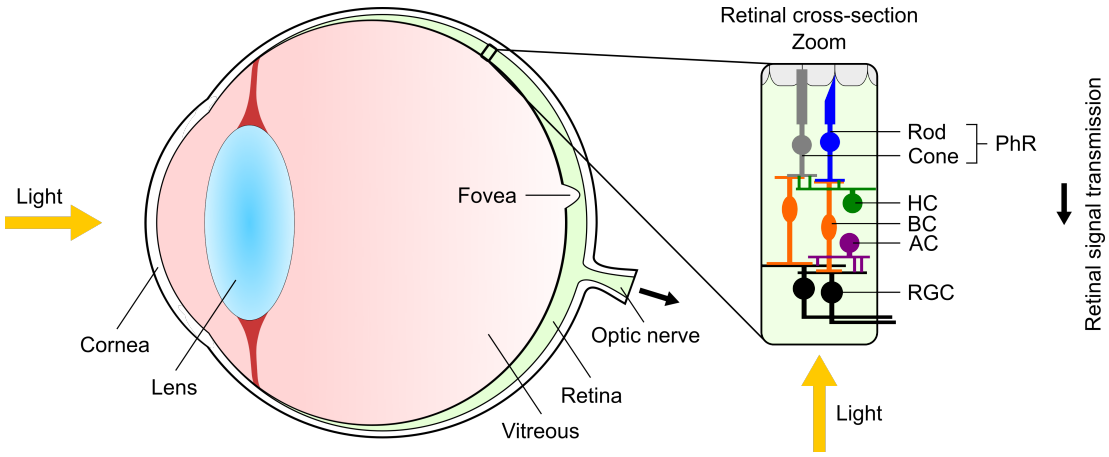

Figure 1.1: Schematic view of the sagittal section of the vertebrate eye and the retina. Abbreviations: PhR: Photoreceptor, HC: Horizontal cell, BC: Bipolar cell, AC: Amacrine cell, RGC: Retinal ganglion cell. Eye schematically drawn after Martinez-Conde (2004), retina schematically adapted from Cepko (2014).

1.1.2 The Retina

The retina is a tissue which performs complex computations. It is composed of specialized neurons, arranged in different layers. The five main functional neuron types are photoreceptors (PhRs), horizontal cells (HCs), bipolar cells (BCs), amacrine cells (ACs) and retinal ganglion cells (RGCs) (for review see (Kolb, 1994; Rodieck, 1998; Gollisch, 2010)). Many of the different neurons which make up the neural layers have first been described by Ramón y Cajal (1892) (for review see Kolb (1994)). Light enters the retina from the RGC layer side, passing the BCs before reaching the PhRs. The PhRs then convert the light signal into neural signals which are transmitted through the BCs to the RGCs. See figure 1.1.
While cones operate at bright light conditions and provide color vision, rods convey variations in light intensity at dim light (Rodieck, 1998; Tortora, 2009; Masland, 2012). There exist two types of BCs, the rod BCs and cone BCs (Hack, 1999). An increase in light (ON) of cone BCs leads to a depolarization of ON-BCs, while a decrease in light (OFF) leads to a depolarization of OFF-BCs (Soucy, 1998). Subsequent stimulation of the RGCs is performed by the excited BCs (Tortora, 2009). Retinal performance is improved through the help of HCs and ACs. HCs provide inhibitory input to the BCs and act as a feedback to the PhRs (Baylor, 1971; Kolb, 1994). The lateral inhibition causes contrast enhancement in the visual scene between strongly and more weakly stimulated, adjacent areas. Further, color differentiation is assisted by HCs (Tortora, 2009). ACs provide inhibitory and excitatory input to the RGCs. ACs also convey the input of the rod-BC to the RGCs. Interactions of ACs in further networks influence and integrate RGC signals (for review see (Kolb, 1994; Rodieck, 1998)). For example, direction selectivity is mediated by starburst ACs (Yoshida, 2001; Euler, 2002; Demb, 2015).
RGCs are the retinal output neurons. They send the signals in the form of action potentials through their axons, which build the optic nerve (Kolb, 1994). They receive inputs from ACs and BCs via chemical synapses and also form electrical synapses with ACs and within each other (Schubert, 2005; Bloomfield, 2009).

About 70.000 RGCs out of an estimation of 117.000 nonvascular cells in the mouse RGC layer were reported in Dräger (1981). With over 8000 $Cells/mm^2$ just temporal to the optic disc, Dräger (1981) reported highest cell density of presumed ganglion cells. A density lower than 2000 $Cells/mm^2$ was shown for the most dorsal retina (Dräger, 1981). Similar values of ~ 8200 $Cells/mm^2$ with a mean value of 117.087 RGC layer neurons were reported in Jeon (1998). Around the retinal center, highest densities are shown with comparatively high densities in the nasal region (Jeon, 1998). While in normal cats, monkeys and humans the RGC number is quite variable (Illing, 1981; Curcio, 1990; Spear, 1996; Jeon, 1998), the difference within mice is only 11 %. While this has an influence on the absolute density, the relative fraction of RGCs in the RGC layer remains the same (Jeon, 1998). The intrinsically photosensitive, melanopsin expressing RGC types M1 and M2 (Hughes, 2013) show a higher density in the dorsal region of the retina (Bleckert, 2014). With about 13 % of the total RGC population in the peak region, the selective feature detector cell, the W3 cell (Zhang, 2012) is stated to be the most numerous RGC type in the mouse retina, on the basis of previous measurements (Jeon, 1998; Zhang, 2012). Populations of other RGC types are lesser than 5 % (Hattar, 2002; Kim, 2008; Huberman, 2008; Yonehara, 2008; Münch, 2009; Huberman, 2009; Kim, 2010; Kay, 2011; Zhang, 2012). In the primate retina, the most numerous RGC type is the Parasol cell (Dacey, 1993; Zhang, 2012).

When compared to other cell types, RGCs vary more within different species, with reason to believe that there are at least 20 RGC types in most species (Masland, 2011). Various groups described and discussed different morphological RGC - classifications. Categorization of Mouse RGCs have been reported with ~ 20 - 22 classes (Sun, 2002; Badea, 2004; Kong, 2005; Coombs, 2006; Völgyi, 2009; Ecker, 2010; Hong, 2011; Zhang, 2012; Farrow, 2013).

Depending on the stimulus provided to the retina, different mechanisms were identified from RGC responses. Based on physiological function and response properties, an early classification was done by Hartline (1983). RGCs can for example be functionally classified into ON-, OFF- and ON-OFF-cells. While ON-cells re-

spond to an increase in light levels, decreasing light levels lead to responses from OFF-cells. ON-OFF-cells respond to both, light increments and decrements (Kolb, 1993; Nelson, 1993; Krishnamoorthy, 2012). Five clusters according to response latency, - duration, relative amplitudes and nonlinearities have been shown in Carcieri (2003). In contrast, clustering with a classification into twelve types was shown in Farrow (2011). A more recent study reported more than 30 functional RGC types in the mouse retina (Baden, 2016). In terms of retinal feature detection, identified mechanisms are for example direction selectivity (Barlow, 1963; Rodieck, 1998; Euler, 2002), object motion sensitivity (Ölveczky, 2003), approach sensitivity (Münch, 2009), local edge detection, uniformity detection and orientation selectivity (Levick, 1967) and motion anticipation (Berry, 1999). Targeting retinal implant related efforts, multiple studies have shown that the remaining retinal circuitry in in-vitro mouse retinas with PhR-degeneration can be used for subretinal E-stim (Stutzki, 2016; Haq, 2018). Further, Sekhar (2017) reported the correspondence between L-stim and E-stim induced RGC input filters.

1.2 Electrical Retinal Implants

Strategies of electrical stimulation (E-stim) of the retina can be employed to evoke visual sensations in blind patients suffering from photoreceptor dystrophy due to retinitis pigmentosa, wherein the degeneration of photoreceptors eventually leads to complete blindness (Bunker, 1984; Hamel, 2006; Hartong, 2006). In retinitis pigmentosa, patients lose sharp vision starting from the retinal periphery. First symptoms are reported as "night blindness", which means that affected people loose their ability to see at night (Rodieck, 1998). In later stages of the disease, patients are either completely blind or they are able to utilize minor fractions of their previous ability to see. E-stim through electrical retinal prostheses can be employed to partially restore lost visual perception. There exist three main kinds of electrical retinal prostheses based on the location of their implantation: Epiretinal implants (Margalit, 2002; Yanai, 2007; Humayun, 2012), suprachoroidal implants (Saunders, 2013; Ayton, 2014; Bloch, 2019) and subretinal implants (Zrenner, 2002, 2010; Mathieson, 2012; Zrenner, 2013; Stingl, 2015, 2017). The subretinal implant (Alpha IMS, Retinal Implant AG, Reutlingen, Germany) has proven to be highly beneficial to blind patients by providing them with visual sensations. In clinical trials, patients claimed to have performed daily tasks, read and combined letters to words and also to have recognized facial expressions (Zrenner, 2010; Stingl, 2015). Figure 1.2 shows different approaches of electrical retinal implants with their respective position of implantation.

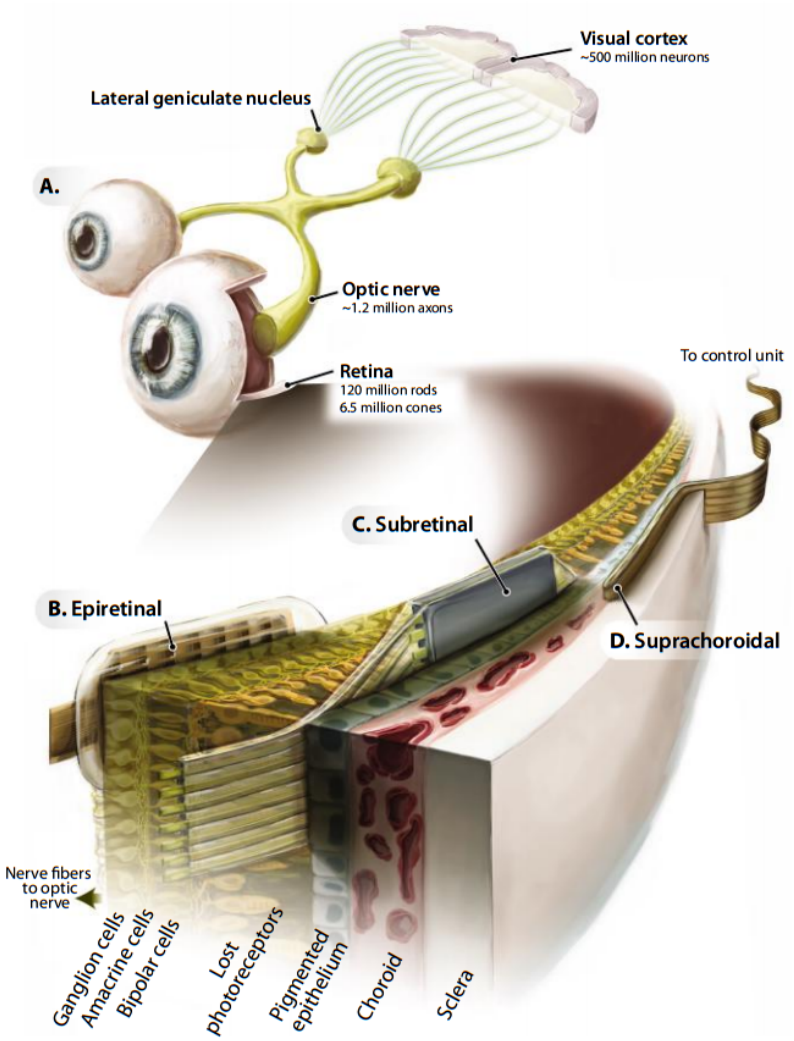

Figure 1.2: Retinal implant approaches. Different approaches of retinal implants with their respective position of implantation: (B) Epiretinal, (C) Subretinal and (D) Suprachoroidal. From E. Zrenner, Fighting Blindness with Microelectronics. Sci. Transl. Med. 5, 210ps16 (2013). Illustration by: CREDIT: V. ALTOUNIAN/SCIENCE TRANSLATIONAL MEDICINE; (Zrenner, 2013).

1.3 Motivation

In this section, the motivational purpose of the thesis is explained with descriptions of the general objectives and the approach. Although present day retinal implants are pioneer works in providing visual sensations to blind patients, there are limitations in providing visual sensations with high spatial and temporal resolution. Reduced spatial resolution presumably depends on the electrode arrangement (Wilke, 2011; Matteucci, 2016), electrode size and electrical pulse duration (Behrend, 2011). Similarly, poor temporal resolution depends on the E-stim parameters (Ryu, 2009; Freeman, 2011; Fornos, 2012). Various comparisons between light-evoked and electrically evoked RGC responses have been discussed in literature, investigating stimulus dependent retinal circuit function and RGC responses on the functional level of single neuron analyses (Baden, 2016). Other works used models of light stimulation to the retina (Warland, 1997; Pillow, 2008; McIntosh, 2016; Maheswaranathan, 2018) considering RGC populations. In terms of retinal implant related research, learning of retina implants was discussed in Eckmiller (2008). E-stim patterns were used to reproduce moving light stimulation (L-stim) induced activity using primate retina (Jepson, 2014). Parthasarathy (2015) decoded natural images from RGC population spiking activity. Shah (2018) showed a neural response metric learned from light induced RGC responses from an RGC population. Another approach is the simulation of visual perception and potential effects of learning with a subretinal implant (Golden, 2019).

An important question in retinal implant vision is, if patients will be able to see objects in their observed visual scene. To date, only the patients can answer this question. In terms of developing a retinal implant to aid vision, this appears to be a very late stage for a qualified feedback. Hence, a data based testing framework was created to estimate the retinal outcome as an early assessment to identify the degree to which the retina has seen the desired object. E-stim induced RGC responses do not comply to light induced RGC responses in a one to one fashion. Therefore this work has great importance for the basic knowledge of retinal signal

coding and -decoding. In particular, the knowledge about redundant content in the retinal response to E-stim can have high impact on further development and efficient E-stim functioning of implants. Considering the spatial resolution of the MEA, this approach gives hints about the redundancy in terms of how much of an object structure is required so that E-stim induced responses can approximate L-stim induced responses to a useful degree. Figure 1.3 depicts the general state-of-the-art approach for the development of new electrical retinal implants. Figure 1.4 shows the proposed procedure for the testing of new developments.

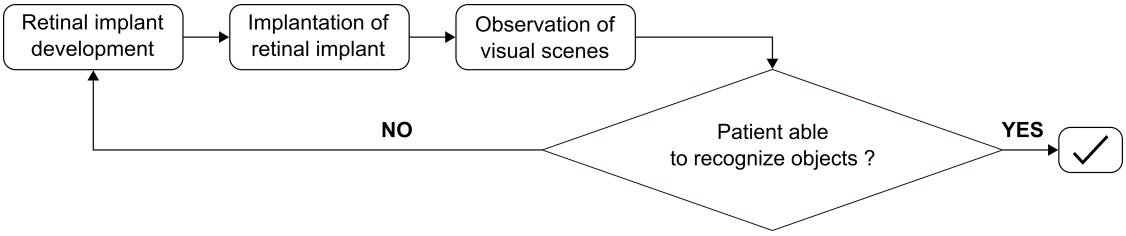

Figure 1.3: Schematic representation of the state-of-the-art procedure for retinal implant tests. After retinal implants are developed and implanted into patients, assessment of the implant function happens through feedback from patients. In the case that patients do not recognize respective objects in their visual scene, retinal implants have to be refined and adjusted based on new developments, in an optimal case influenced by the patient feedback. New developments consider parameters such as implant materials, electrode types, the arrangement of electrodes and different stimulation strategies.

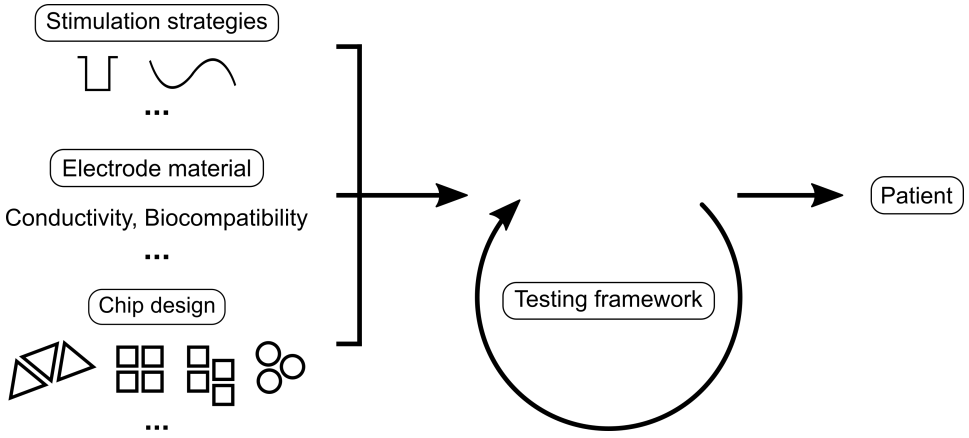

Figure 1.4: Schematic of the proposed procedure for testing new developments. New developments for retinal implants can be tested using the proposed data-based testing framework, before starting clinical trials with patients. New developments contain spatio-temporal electrical stimulation (E-stim) strategies, implant materials aiming for miniaturization and highly conductive materials with good biocompatibility, types and arrangement of electrodes and other implant chip features. Using the testing framework, engineering loops could be shortened drastically.

1.3.1 Objectives & Approach

A decoding framework on the basis of a convolutional neural network (CNN, see (Bishop, 2006; LeCun, 2015)), a form of artificial neural networks (ANNs) shall be developed to achieve functional benchmarking for E-stim evoked RGC responses. To asses E-stim induced RGC responses in terms of efficient stimulation strategies, CNNs trained on L-stim induced responses shall be used as a reference. To date, multiple cells are stimulated simultaneously through implant electrodes. In accordance to this, this work shall cover the signal derivation of multiple cells at one electrode, which can be thought of a convolutional process during recording. In this work, the whole retinal read out shall be considered in the form of an input-output relationship, without focus on internal retinal mechanisms, as for example in Maheswaranathan (2018) and also in contrast to analyses based on single cell function, as for example in (Chichilnisky, 2001; Baden, 2016). In the interest of blind patients, a black-box approach on the meta-level is described. This can be achieved through multielectrode recordings of stimulation induced RGC responses. Pattern recognition of E-stim induced RGC responses should be performed with a

specially acquired L-stim induced response library (LRL). This LRL can be used for training ANNs which can then be employed to test E-stim induced RGC responses. A schematic representation of the proposed approach elaborated in this work is shown in figure 1.5.

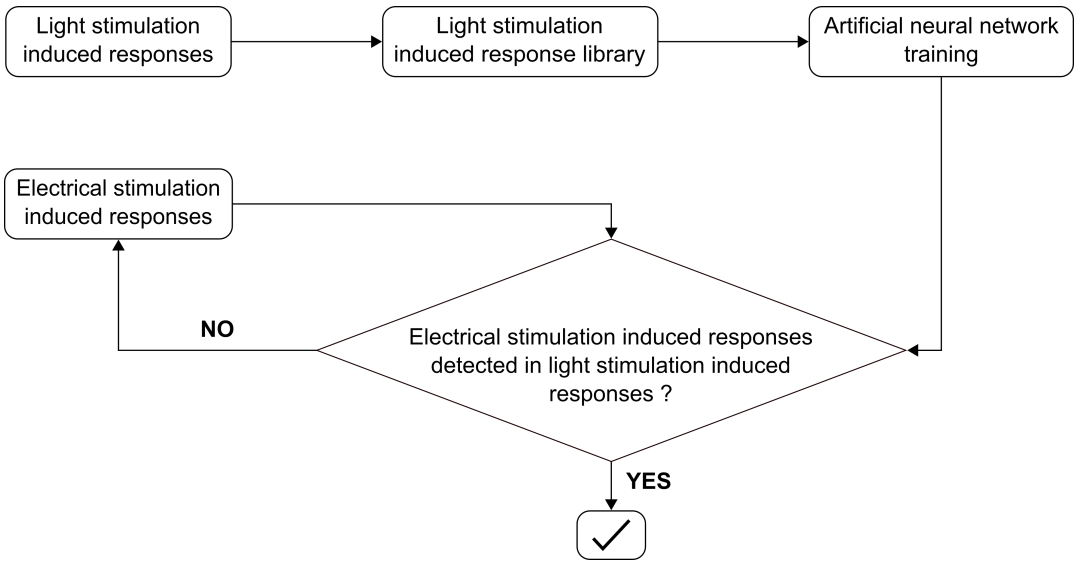

Figure 1.5: Proposed Approach. Light stimulation (L-stim) induced retinal ganglion cell (RGC) responses are used to build up a light stimulation induced response library (LRL) with different classes. Artificial neural networks (ANNs) are then trained with the LRL. Electrical stimulation (E-stim) induced RGC responses are then used as test data with the ANNs trained on the LRL, to test whether the ANNs can classify the E-stim induced responses correctly. Based on the classification output, new E-stim patterns can be designed in an iterative procedure, if required. An important ascpect in this approach is the fact that E-stim induced RGC responses are not used for ANN training at any point of time. E-stim induced RGC responses are exclusively used as test data, held out data, respectively.

Chapter 2

Methods

This chapter describes the experimental set-up, followed by methodological procedures for recording extracellular RGC responses based on light stimulation (L-stim) and electrical stimulation (E-stim). The chapter also includes descriptions of the general data processing and the artificial neural network (ANN) based approach.

2.1 Electro-Physiological Experimental Set-Up

For retinal prostheses research, MEA technology provides a suitable environment for stimulation and recording purposes. In such measurements, various parameters can affect recording quality, and therefore the quality of the data used for further processing. Among others, important factors are the retinal dissection procedure and therefore the nature of the tissue, tissue-electrode interaction and tissue adaptation. For data acquisition, the MEA60 system (Multi Channel Systems MCS GmbH, Reutlingen, Germany (MCS)) was used with the Software MC_Rack (MCS) to record with all electrodes in parallel. RGC responses were recorded at a sampling rate of 25 kHz. For L-stim, a custom built light path in combination with an upright microscope (BX50WI, Olympus K.K., Tokyo, Japan) was used (figure 2.1). Two cameras were used for control and calibration measures. The planar, hexagonal MEA consisted of 59 circular titanium nitride (TiN) electrodes of diameter = 10 μm and had an inter-electrode spacing in x and y directions of 40 μm. The mean impedance of the electrodes was measured to be 0.7 MOhm. Before and after every experiment, the MEA impedance was measured using nanoZ (MCS).

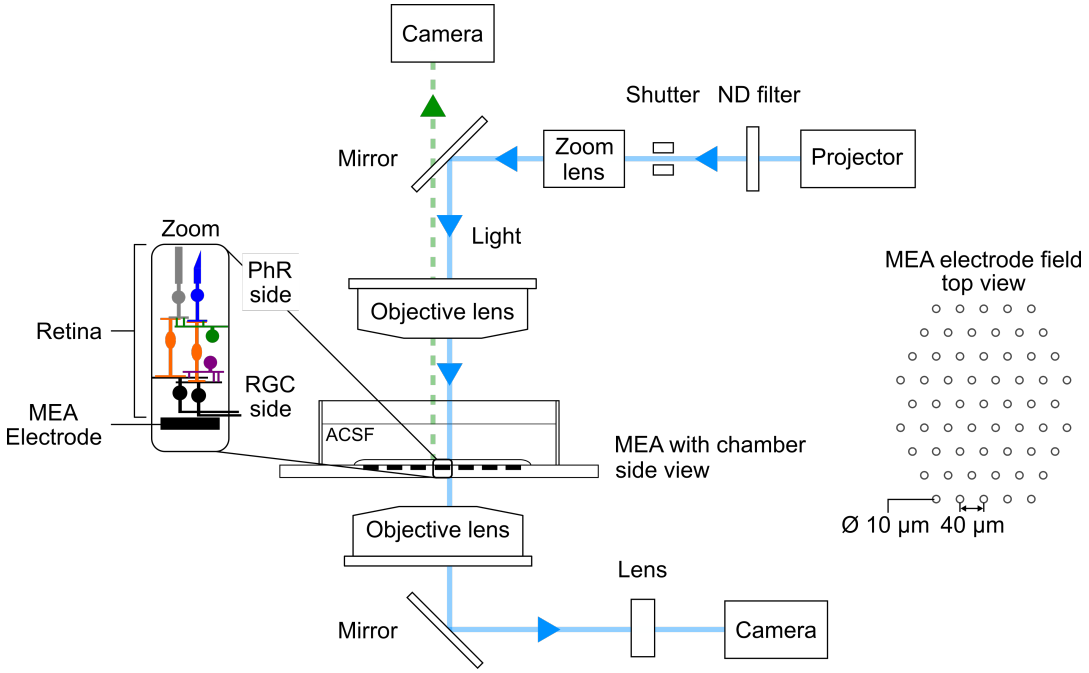

Figure 2.1: Schematic representation of the multielectrode recording setup. A projector based light stimulation (L-stim) of retinal tissue on the multielectrode array (MEA) is shown. Electrical stimulation (E-stim) can be presented through the MEA electrodes. MEA electrodes are used for recording extracellular retinal ganglion cell (RGC) responses. Top view of the MEA electrode field (59 electrodes in hexagonal arrangement) is shown on the right side. Further abbreviations: PhR: Photoreceptor; ACSF: Artificial cerebrospinal fluid. ND: Neutral density. (Basavaraju S, Speck A, et al., in preparation).

2.2 Multielectrode Stimulation & Recordings

2.2.1 Animal Tissues

Using retinal tissues from mice as the crucial data source in this work, one has to take certain comparisons to the human retina into account. Mice do not have a fovea, so the whole mouse retina can be compared to primate peripheral vision (Krishnamoorthy, 2012). Further, there is a high similarity between the visual sensitivity of the human peripheral retina and the visual sensitivity of the mouse (Naarendorp, 2010). Cells in the mouse retina are almost uniformly spaced across the retina in a given mosaic (Roska, 2014). The independency of retinal location and eccentricity is therefore a great advantage for RGC recordings (Krishnamoorthy, 2012) in this work.

2.2.2 Tissue Sample Preparation

For MEA recordings, healthy wild type mice (C57BL/6, Jackson Laboratory, Bar Harbor, ME, USA) with ages ranging from 3 to 8 weeks were used. Mice were kept in a normal day/night cycle environment with access to water and food. All efforts to minimize the number of mice were made. The procedures were approved and supervised by the Tübingen University commitee on animal protection (Einrichtung für Tierschutz, Tierärztlicher Dienst und Labortierkunde; Tierschutzgesetz). Experimental procedures were performed in accordance with the ARVO statement for the use of animals in ophthalmic and vision research. Mice were anesthetized deeply by inhalation of carbon dioxide, after which they were euthanized by cervical dislocation. Then the eyes were removed under dim light conditions and dissected under dim red light illumination in artificial cerebrospinal fluid (ACSF) containing (in mM): 125 NaCl, 2.5 KCl, 2 CaCl2, 1 MgCl2, 1.25 NaH2PO4, 26 NaHCO3 and 20 Glucose; pH 7.4. To isolate the retinal tissues, eyes were hemisected and the lens and vitreous were removed, before removing the pigment epithelium. Care

was taken not to damage the retinal tissues. Retinas were then cut into multiple pieces, to increase the number of measurements and therefore to account for variance, also considering the 3R-practice (Russel, 1959). Retinal pieces were handled through forceps, exclusively touching the tissues at the rim or at the cut sides, whereas areas chosen for recording were not touched with the forceps.

2.2.3 Recording Procedure

Under microscopic control, retinal pieces were mounted on a hexagonal MEA with high electrode density (Hex MEA (MCS)), with the RGC side oriented down, facing the MEA (similar to the procedures in Berry (1999)). The MEA was located inside a well which was superfused with carbogenated ACSF at 1 ml/min ((Stett, 2000), perfusion rate) and ~ 32 °C using the peristatlic perfusion system PPS2 and the temperature controller TC02, respectively (MCS). At the beginning of each experiment, L-stim flashes were presented to the retina to check for tissue-electrode contact and recording quality. Stimuli contained five ON-OFF cycles with 2 s ON at 35 cd/m^2 and 2 s OFF at 1 cd/m^2. Only recordings with at least 90 % of electrodes containing responses were considered, after which the retinal tissue was kept on the MEA for at least 60 min before starting the measurements to account for tissue adaptation. Remaining tissues were kept in ACSF and carbogenated until needed.

2.2.4 Stimulation Patterns

Light Stimulation

L-stim patterns were generated using custom made MATLAB (The MathWorks, Inc., Natick, MA, USA (TMW)) scripts, employing psychtoolbox (Brainard, 1997; Pelli, 1997) functions. The L-stim software was incorporated into a graphical user interface (figure 2.3). Trigger signals were controlled through NI USB - 6000

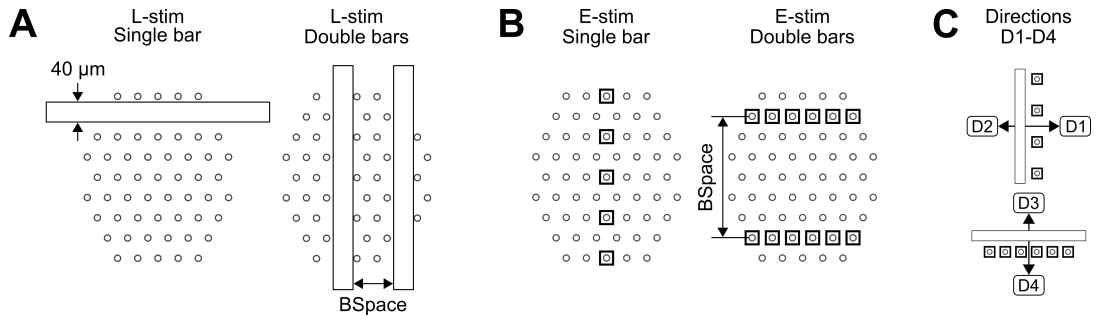

Figure 2.2: Schematic representation of the light stimulation and electrical stimulation patterns. (A) Light stimulation (L-stim) patterns consisting of single or double bars with bar spacing BSpace = 40, 80, 120, 160, 200, 240, 280, 320 μm and velocity v = 100, 220, 330, 400, 450, 550, 600, 700 $\mu m/s$ moving in four directions D1-D4 across the retina on the multielectrode array (MEA); Bar thickness = 40 μm. (B) Electrical stimulation (E-stim) patterns as single or double bars can be produced through the MEA electrodes. Retinal tissue not shown. Electrode diameter: 10 μm; Electrode spacing: 40 μm.

(National Instruments Corp., Austin, TX, USA) with MATLAB (TMW). An automatic shutter using a servo motor drive and an Arduino Uno (Arduino SA, Chiasso, Switzerland) microcontroller was built in between the light pathway to block background light from the projector falling onto the retina when required. L-stim intensities were adjusted to a luminance of 35 cd/m^2, with a background luminance of 1 cd/m^2. A luminance level of 35 cd/m^2 is at the lower end of the photopic vision range (Tanimoto, 2013; Tsai, 2017). L-stim patterns were presented as horizontal single bars or as double bars (bar orientation as in Berry (1999)) with different bar spacing (BSpace = 40, 80, 120, 160, 200, 240, 280, 320 μm, figure 2.2 (A)), moving at various velocities (v = 100, 220, 330, 400, 450, 550, 600, 700 $\mu m/s$) in four directions (D1 - D4, figure 2.2 (C)) across the retinal tissue placed on the MEA. Based on these measurements, a preliminary dataset of 48 classes was used for first evaluations. A combination of all the parameters (Single bar, double bar with BSpace, v, D) leads to a dataset of 104 classes with ~ 1800 single measurements. A single recording-run consisted of: A bar type (single or double) moving 10 times (with 10 s inter-stimulus pause) across the retina in one direction at a particular velocity. The classes obtained were organized in a light stimulation induced response library (LRL). Additional information: Building on the preliminary analyses, an original dataset including an additional four directions

(alltogether D1 ... D8) was collected with more than 2000 single measurements.

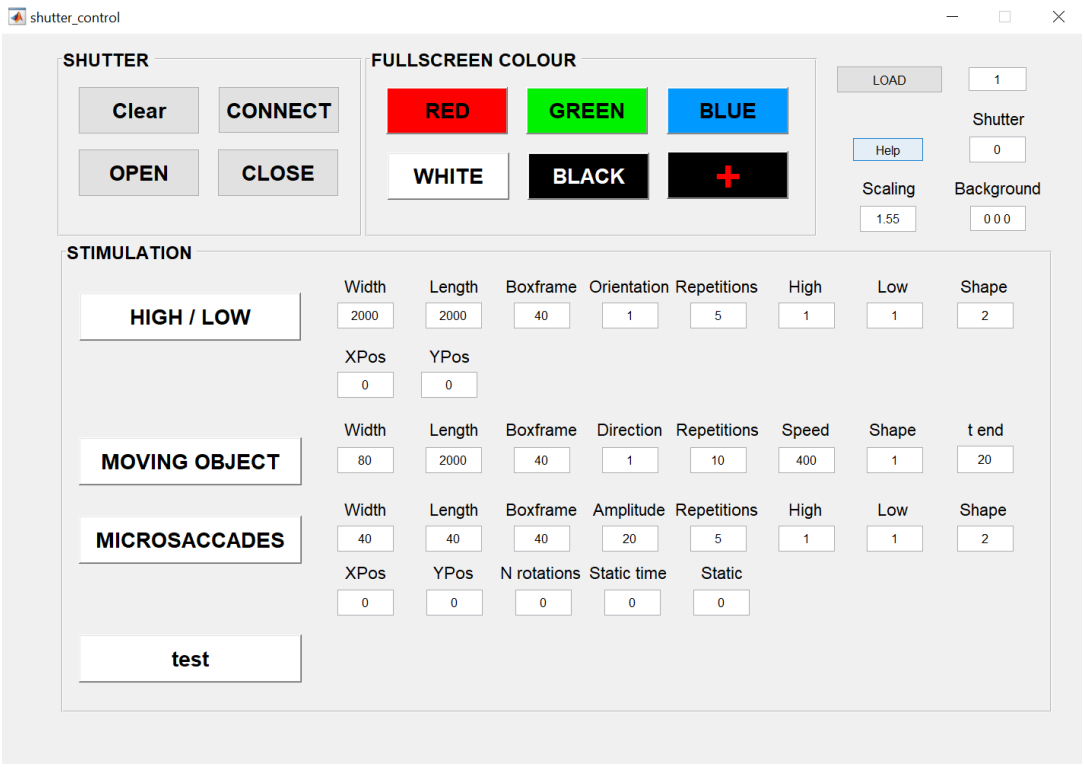

Figure 2.3: Graphical user interface for light stimulation control. Different stimulation patterns can be defined through various parameters. The user interface employs MATLAB (TMW) based algorithms, implementing psychtoolbox (Brainard, 1997; Pelli, 1997) functions. This user interface was developed in collaboration with Sunetra Basavaraju.

Electrical Stimulation

E-stim patterns were presented through the MEA electrodes, with the signal generator STG2008 (MCS). Software used to program E-stim patterns were MC_Stimulus II and MEA_Select (MCS). Stimulation strengths for E-stim were designed under the general consideration of the following keypoints: Stimulation strengths should not exceed certain limits, to avoid damaging the retinal tissue and the electrodes of the MEA. E-stim induced RGC responses should be induced with proximity to the stimulation electrode, therefore achieving local stimulation with as much as possible control in locations of interest. To understand the operational limits of the MEA system during E-stim and to procure an E-stim strength suitable for the experiments, preliminary tests were conducted.

Retinal tissue was stimulated using a single electrode presenting monomodal cathodic E-stim strengths; -100, -300, -500, -700, -1000, -1200, -1500, -1700, -2000, -2200, -2500, -2700, -3000 mV and the pulse duration was set to 0.5 ms. Each E-stim pattern consisted of an E-stim pulse strength which was repeated 10 times with an interpulse interval of 10 s. RGC responses were recorded using the rest of the MEA electrodes.

In analog to the L-stim patterns, E-stim patterns consisted of single or double bars with bar spacing BSpace = 40 μm and 240 μm and velocity v = 220 μm and 550 $\mu m/s$ moving in four directions D1-D4 across the retina presented by the electrodes of the MEA (see figure 2.2 (B) and (C)). One recording-run consisted of 20 repetitions with 10 s of wait time between each repetition of a particular selected bar type, at a certain velocity and in one of the four directions. In particular, the classes were as follows: Single bar x 2 velocities + double bars with 2 BSpaces x 2 velocities times 4 directions = [2 + 4] x 4 = 24. Based on this, an E-stim induced response library (ERL) with 24 response classes including more than 400 single measurements was used.

2.3 Data Processing

Recorded data were high pass filtered with a 2 pole butterworth filter at 200 Hz in MC_Rack (MCS) and then saved in HDF5 file format. "McsMatlabDataTools" (MCS) was used to read HDF5 files in MATLAB (TMW). Further data processing and the respective analyses were performed using custom written MATLAB (TMW) scripts. Also the ANNs were used with MATLAB (TMW). Unless mentioned otherwise, RGC responses were binned at 100 ms. Respective response frequencies were then calculated. For the time course analysis of activity recorded from single electrodes, gaussian fits with the MATLAB (TMW) function lsqcurvefit were used (figure 3.4 (B)). The parameters of the gaussian fit with the function

$$f(x) = a * e^{-\frac{(x-b)^2}{2c^2}} \tag{2.1}$$

were used to describe the different characteristics of the responses. The parameters a, b and c^2 are non-zero constants representing the height of the curve's peak, the center position of the peak and the width of the curve (variance σ^2) respectively. For the intended tasks in this work and the implicated analyses, retinal tissue samples were not oriented specifically. Regarding this aspect, the points mentioned in chapter 2.2.1, page 15 were critically taken into account.
To ensure that directional preference and MEA recording location did not influence the analysis in this matter, a direction selective index (DSI) was calculated with

$$DSI = \frac{direction_{pref} - direction_{null}}{direction_{pref} + direction_{null}} \tag{2.2}$$

after (Elstrott, 2008; Mazurek, 2014), but for each recording electrode to get an estimate of the directional preference of retinal tissues to certain stimulus directions. Recordings with DSI > 0.6 were considered direction selective (as described for cells in Elstrott (2008)). DSI values were calculated for the responses recorded at each electrode. For this analysis, L-stim single bars and E-stim single bars with directions D1 to D4 and a velocity of v = 220 $\mu m/s$ were used.

Specific processing of data for other particular analyses is indicated in the respective chapters in the thesis.

2.4 Artificial Neural Network based Object Discrimination

The intention of this step is to employ ANNs, generally following the principle of using ANN models which sufficiently solve the problem without an increased cost of complexity. Figure 2.4 shows the general procedure for the comparison of L-stim induced RGC responses and E-stim induced RGC responses. A hardlimit function was applied to the RGC response sequence matrices, to obtain binary matrices. Classes were defined based on the applied stimulation patterns, and checked through additional supervision during and after recordings, using MC_Rack (MCS).

2.4.1 Artificial Neural Network Architecture & Training

Pre-Evaluation of Light Stimulation induced Responses

In this approach, response sequence matrices contained spatio-temporal components of the recorded RGC responses in two dimensions. In order to build a fundamental understanding of the dataset, a three-layer ANN with one hidden layer (HL) and feedforward architecture was applied, varying the number of neurons in the HL to achieve a sufficient approximation for a dataset of 48 L-stim (Speck, 2018) induced response classes. See Cybenko (1989) for approximations using ANNs with single HLs and sigmoidal nonlinearities. See Bishop (2006) for more details on ANNs. To account for practicalness, different RGC types were not considered in particular, since in this work the whole population information is considered without applying spike sorting techniques. Typically, with the used system configuration, signals from one RGC were recorded at one recording electrode. Here, the possibility to record RGC spike signals from one cell at multiple electrodes is a rare case, too (personal laboratory communication, other dataset, (Haq, 2018)). Only biphasic spikes were considered in the analysis (Haq, 2018).

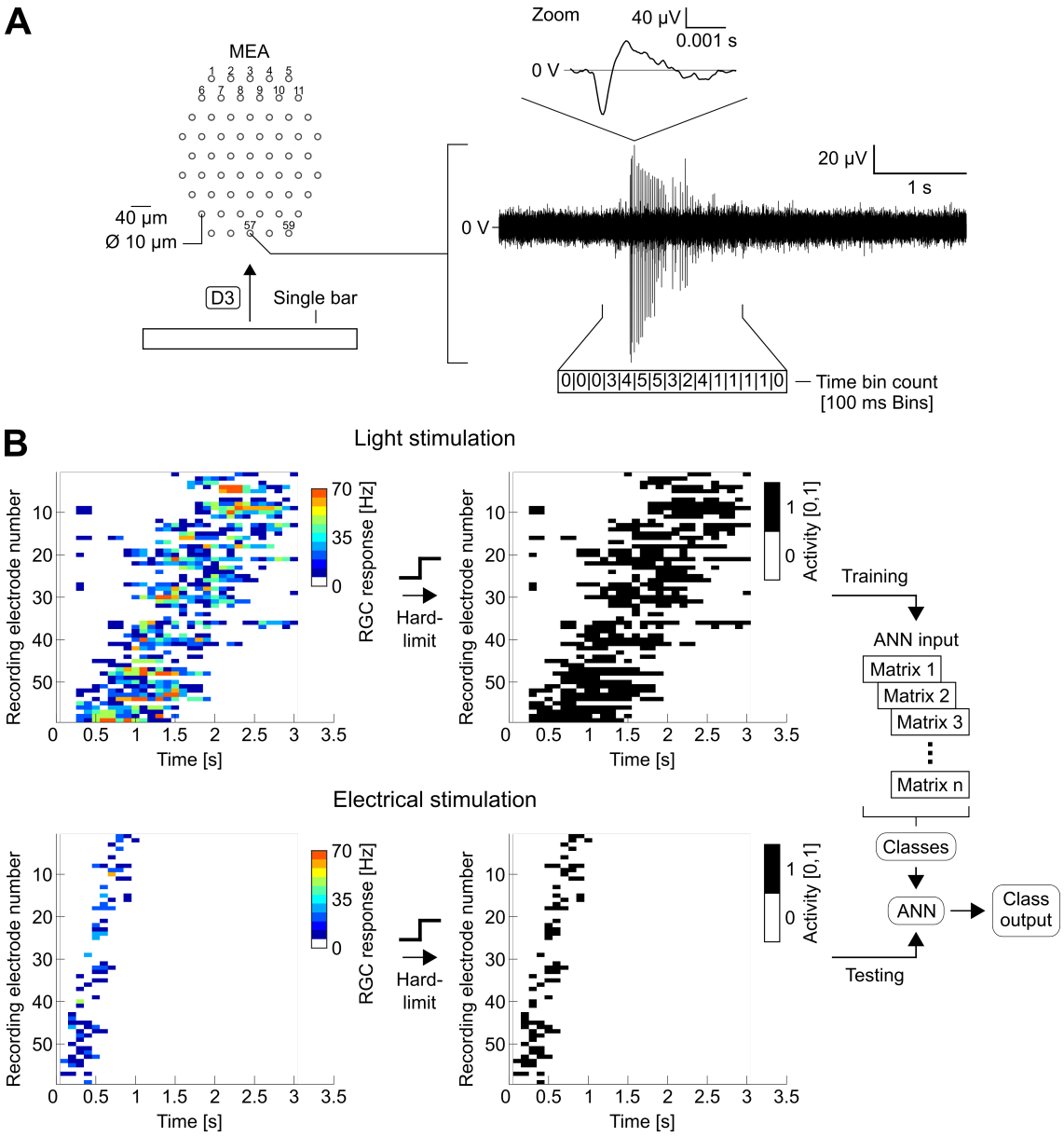

Figure 2.4: Data processing for artificial neural network based classification. (A) Top view of a moving single bar light stimulus along direction D3 and the multielectrode array (MEA) recording field with an example of an extracellular retinal ganglion cell (RGC) response recorded at electrode 57, high pass filtered at 200 Hz; retinal tissue not shown. Zoom section shows an RGC spike. Spike detection declared at different thresholds. (B) Further processing for each electrode signal using binning with a time bin size (TBS) of 100 *ms* of which the RGC response can be obtained. Applying a hardlimit function yields a binary matrix for each measurement. Obtained matrices are organized in respective classes and used for training artificial neural networks (ANNs).

Network input consisted of binary RGC signals from all MEA electrodes, where time-bins containing RGC events are indicated with a "1", else with a "0".

$$f(x) = \begin{cases} 1 & \text{for } N_{events} >= 1 \\ 0 & \text{else} \end{cases} \tag{2.3}$$

The fraction of false classifications was evaluated for different temporal resolutions by using time bin sizes of TBS = 0.1 s, 0.2 s, 0.3 s, 0.5 s, 0.7 s and 1.0 s, in dependence on the number of neurons in the HL, to find a suitable number of HL neurons. The $N_{classes} = 48$ classes dataset consists of $N_{sequences} = 720$ single sequences of length $L_{sequence} = 6$ s with $N_{electrodes} = 59$ recording electrodes, leading to an input matrix

$$I = \begin{bmatrix} R & N_{sequences} \end{bmatrix} \tag{2.4}$$

with

$$R = N_{electrodes} * \frac{L_{sequence}}{TBS} \tag{2.5}$$

The underlying principle for pre-evaluation is schematically shown in figure 2.5. Data were randomly seperated into data for train = 75 %, validation = 15 % and test = 15 %. The networks were trained with scaled conjugate gradient (Moller, 1993) backpropagation and network performance was cross-entropy. The target matrix T consists of $N_{sequences} = 720$ unit vectors from the identity matrix $I_N = diag(1, ..., N)$ with a 1 in the row which represents the respective class.

Convolutional Neural Network based Analysis

A convolutional neural network (CNN, see (Bishop, 2006; LeCun, 2015)) was employed for the test networks of reference. Since the data consists of time series of events, namely the RGC activity over time for each MEA channel, it was possible to treat data matrices as images, with the axes being electrodes over time, con-

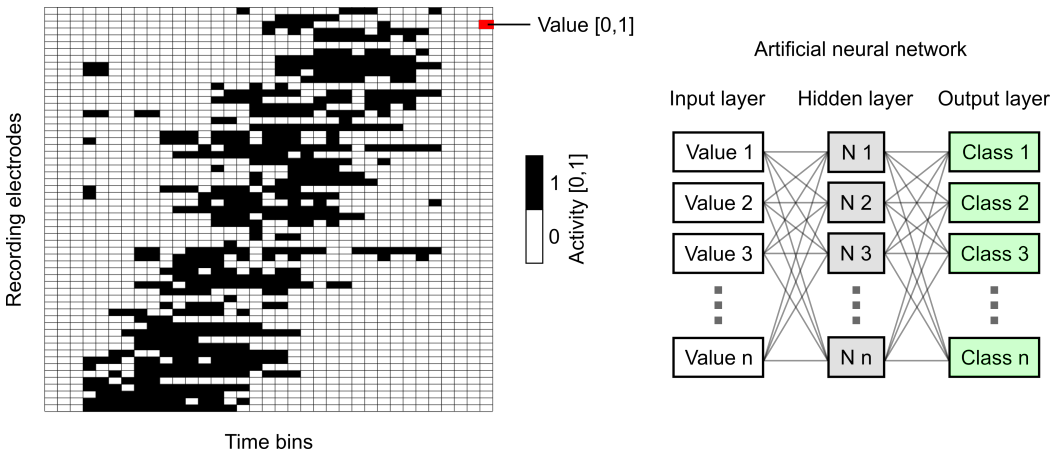

Figure 2.5: Schematic of the underlying principle for pre-evaluation. Binary retinal ganglion cell (RGC) responses as avtivity [0,1] matrices from all recording electrodes are shown in response matrices as single recording sequences, for a time course of multiple seconds. The size of a matrix is therefore defined through the number of recording electrodes, the recording duration and the time bin size (TBS). RGC response matrices are used to train and test a feedforward artificial neural network (ANN) with one hidden layer.

stituting spatio-temporal information of the induced RGC responses. Although with another approach, using time series data transformed to images was used in Wang (2015). In the approach shown here, the resolution of a matrix was defined in dependence on the number of recording electrodes, the TBS and the recording duration. Therefore a matrix was defined as described through the previous equations. The choice for treating the data as image matrices is based on the fact that recorded sequences can be captured within few seconds to achieve an environment with comparable response classes with a fast and simple training procedure. Further, using CNNs, no feature extraction has to be performed, as the network learns the features from the training input data. Visualizations of the learned features can give important insights for stimulus design and clues for the optimization of CNN parameters. A schematic network architecture is shown in figure 2.6.

Generally, the cross-entropy error function

$$E = -\sum_{i=1}^{N_{samples}} \sum_{j=1}^{N_{classes}} t_{ij} ln(x_{ij}) \tag{2.6}$$

and the softmax function

$$y_i = \frac{\exp(x_i)}{\sum_{j=1}^{N_{classes}} exp(x_j)} \tag{2.7}$$

with $0 \leq yi \leq 1$ and $\sum_{i=1}^{N_{classes}} y_i = 1$ were used, implying softmax probabilities being in the range [0 ... 1] and the sum of all the probabilities in the respective case is equal to 1. See Bishop (2006) for further explanations.

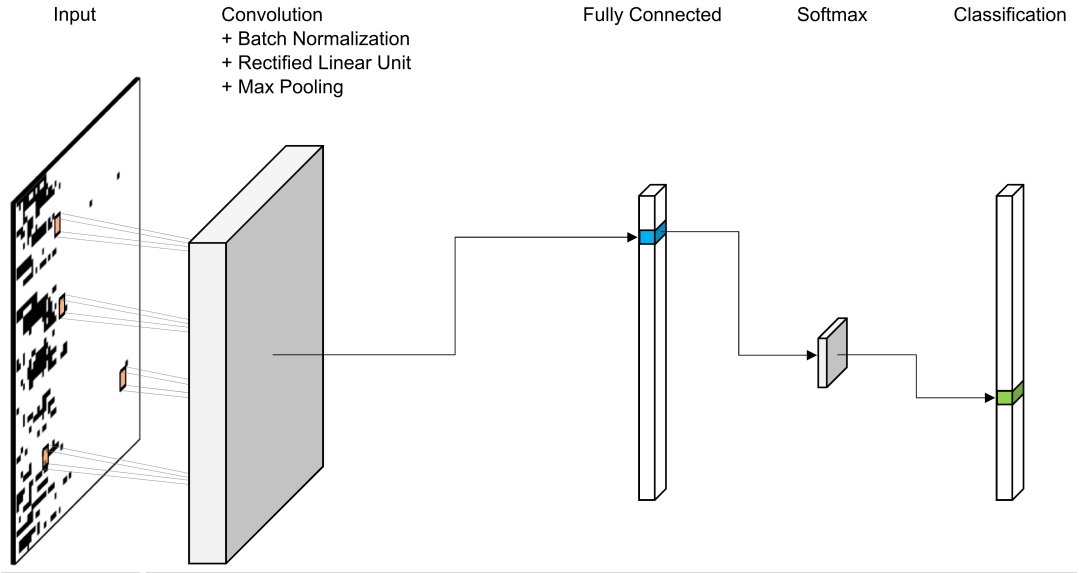

Figure 2.6: Schematic convolutional artificial neural network layout. Data matrices are used as network input followed by convolurional layer, fully connected layer, softmax layer and the classification layer.

The number of convolutional layers, the size and the number of filters in different configurations were varied. Performance optimization was achieved through variations of mini-batch size, the number of maximal epochs and input size. Data was randomly split into 70 % for training and 30 % for validation. For testing with held out data which the network has not seen before, epiretinal electrically induced RGC responses were used. Evaluation of E-stim induced response classifications was performed using different measures such as performance analyses based on sensitivity, specificity and overall accuracy. As test data, in each run single electrically induced responses were randomly chosen from the E-stim induced response library (ERL). This was repeated over multiple trials to estimate the robustness of the classifications for the respective configurations. For the tested architecture, increasing the number of convolutional layers to more than one, did not increase classification accuracy. Different networks were trained and tested with different constellations of training classes, named Sets. See figure 3.15 (A) for different Sets. See chapter 3.2.2, page 45 for a direct result-based evaluation.

Chapter 3

Results

This chapter shows the results for the respective sections. Chapter 3.1 contains the results for the retinal ganglion cell (RGC) response characteristics, with special attention on the spatial spread of RGC responses. Chapter 3.2 incorporates the results for the assessment of electrical stimulation (E-stim) induced RGC responses with artificial neural networks (ANNs), trained with light stimulation (L-stim) induced responses.

3.1 Stimulus-Dependent Retinal Ganglion Cell Responses

In the following, results obtained from respective analyses regarding RGC response characteristics are shown. The first part shows responses to light flash stimulation. For spatial spread and time course analyses of RGC responses, part 2 shows respective results. Results for direction selective activity are shown in part 3, followed by results for the stimulus anticipation analysis in part 4.

3.1.1 Responses to Light Flash Stimulation

At the beginning of each experiment, light flashes were presented to the retina to check for tissue-electrode contact and recording quality. Example RGC responses are shown in figure 3.1 (A), for one electrode. The responses show a clear time-correlation to the L-stim flashes, with bursts of RGC spikes in response to ON-stimuli (2 s, 35 cd/m^2) as the rising edge, and more narrwow shaped RGC responses in reaction to the falling edges, being the OFF-stimuli (2 s, 1 cd/m^2). Only recordings with at least 90 % of electrodes that contained RGC responses were considered (overall exclusion ~ 10 %). Figure 3.1 (B) shows an example of a recording with 100 % of the electrodes showing good electrode contact. RGC responses are here shown for two ON/OFF cycles as the number of spikes per time bin. Examples for locations with a relatively low RGC response level are indicated by the blue boxes. Regardless the low response level, these signals are still considered useful, as the responses can not be expected to be identical for all locations. RGC response levels are influenced by parameters such as tissue condition, tissue-electrode contact and RGC type. An example with a higher RGC response level is indicated by the green box.

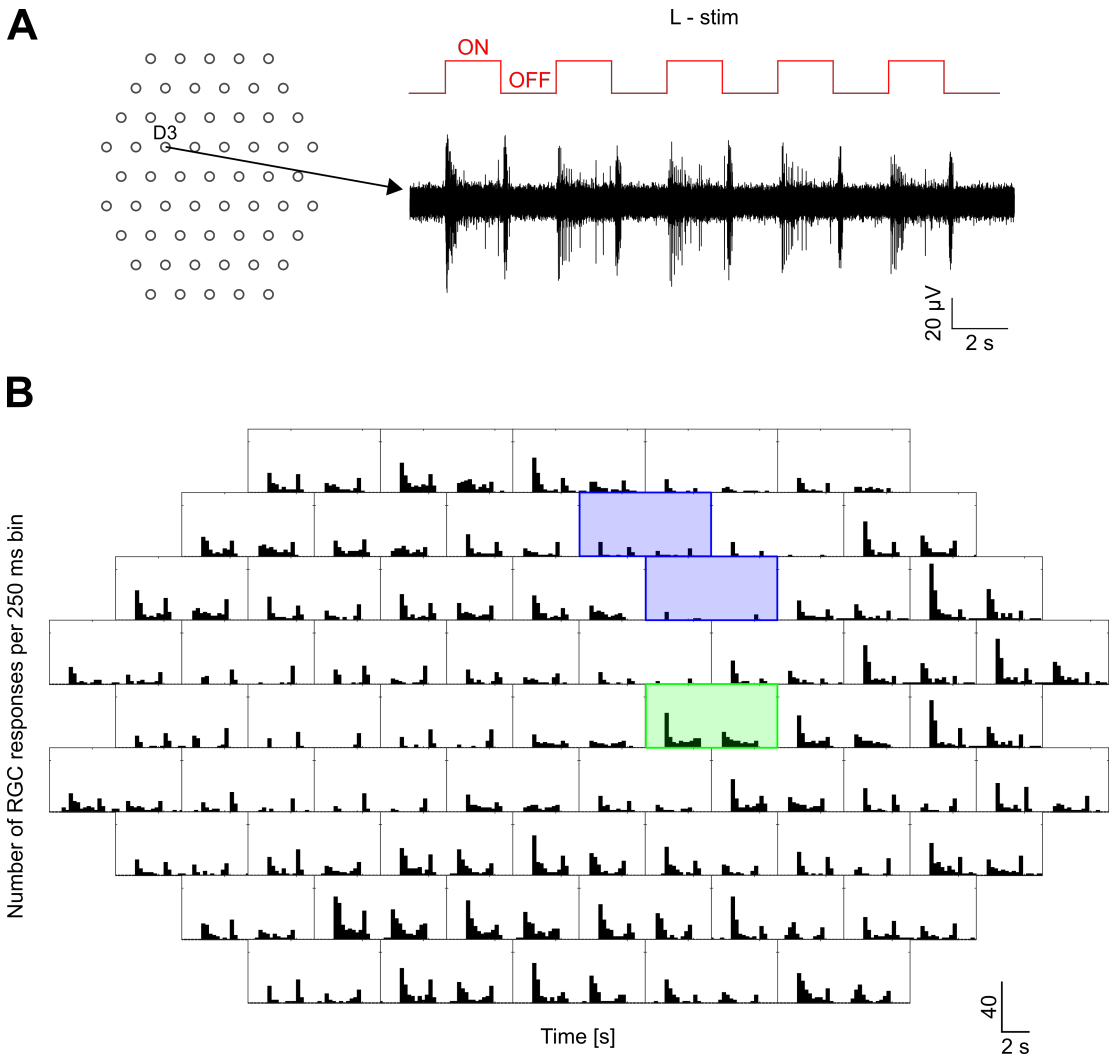

Figure 3.1: Responses to light flash stimulation. (A) Multielectrode array (MEA) and ON/OFF light stimulation (L-stim) with respective L-stim induced retinal ganglion cell (RGC) responses obtained on electrode D3. Stimuli contained five ON-OFF cycles with 2 s ON at 35 cd/m^2 and 2 s OFF at 1 cd/m^2. Retinal tissue not shown. Electrode diameter: 10 μm; Electrode spacing: 40 μm. (B) RGC Responses at all MEA electrodes. Responses for two ON/OFF cycles are shown. Two recording electrodes with a relatively low RGC response level are indicated by blue boxes. Although these two electrodes do not show a high response level, the recorded responses are useful. As comparison an example with a higher RGC response level is indicated by the green box.

3.1.2 Spatial Spread & Time Course of Responses

RGC response spread dependent on single electrode E-stim strengths was analyzed in experiments using stimulation strengths of -100 to -3000 mV at a pulse width of 0.5 ms. As a reference, a threshold was defined as 25 % of recording electrodes in the respective spatial bin (Basavaraju S, Speck A, et al., in preparation). Strengths from -100 to -700 mV show a smaller fraction of responses when compared to the stimulation strengths of -1000 to -3000 mV. At 40 μm spatial bin, the normalized number of recording electrodes (NR) reached the 25 % threshold with an average of 26.67±8.31 % for a stimulation strength of -700 mV. For E-stim strengths of -1000 mV to -1700 mV, the NR reduced with an increase in distance from 40 μm to 120 μm. At -1000 mV the NR at 40 μm and 80 μm bin was observed to be 45.33±9.42 % and 12.67±3.83 % respectively. For a strength of -1200 mV, the NR at 40 μm and 80 μm bin was observed to be 50±9.37 % and 17.86±5.36 % respectively. The values at 120 μm and 160 μm bins were observed to be lower than 25 %. For E-stim strength of -2000 mV to -3000 mV the NR cross the 25 % threshold at a farthest bin of 160 μm, in most cases.

Generally, increasing the E-stim strength results in a higher spatial spread of responses, as indicated by the NR in the respective bin. Since there was no crucial increase in the number of response containing electrodes between -1000 mV and -1200 mV at the distances of interest, being 40 μm and 80 μm, an E-stim strength of -1000 mV was chosen for the main experiments (in accordance with Haq (2018) for subretinal E-stim).

E-stim experiments were then conducted at a voltage strength of cathodic -1000 mV with a pulse duration of 0.5 ms based on preliminary experiments and on electrode safe charge data provided by MCS. In the MEA system used, it was observed that stimulating with the same electrode on an average of 10 times with 10 s interpulse interval, recording RGC responses from the stimulation electrode was possible. In accordance with this observation, E-stim moving-bar experiments were performed with 20 stimulation sequences to achieve a conditioning effect.

Light induced RGC responses show a generally larger response time course when compared to E-stim induced responses with a ratio of ~ 3:1.5 s. Figure 3.2 shows examples of L-stim induced RGC responses to single bars moving in directions D1-D4. Examples of respective E-stim induced RGC responses to single bars moving in directions D1-D4 are shown in figure 3.3. Moving the stimulus in any of the four directions leads to clear distinguishable response timings.

The RGC responses induced through epiretinal E-stim show a generally lower RGC response level with a maximum of 10 Hz when compared to the L-stim induced RGC responses with a maximum of 40 Hz. E-stim with directions D1 and D2 (figure 3.3 (A)) are activated in a more sparse configuration (inter-electrode distance = 80 μm, for example see figure 2.2 (B), E-stim with a single bar) when compared to E-stim with directions D3 and D4 (inter-electrode distance = 40 μm, figure 3.3 (B)). The differences in electrode activation for E-stim is based on the electrode arrangement, the MEA layout respectively.

With a stimulus velocity of v = 220 $\mu m/s$, the stimulus crosses the MEA in 1.3 s for D1 and D2, and in 1.5 s for D3 and D4. Respective L-stim and E-stim responses in spatio-temporal correlation to the stimulus are described below for a direct comparison:

1. L-stim. The responses appear with a clearly longer time course (~ 3 s) as the stimulation time (~ 1.3 s), with a difference of ~ 1.7 s. See discussion in chapter 4.1.1

2. E-stim. The response time courses (~ 1.3 s) are observed to last approximately as long as the E-stim (~ 1.3 s).

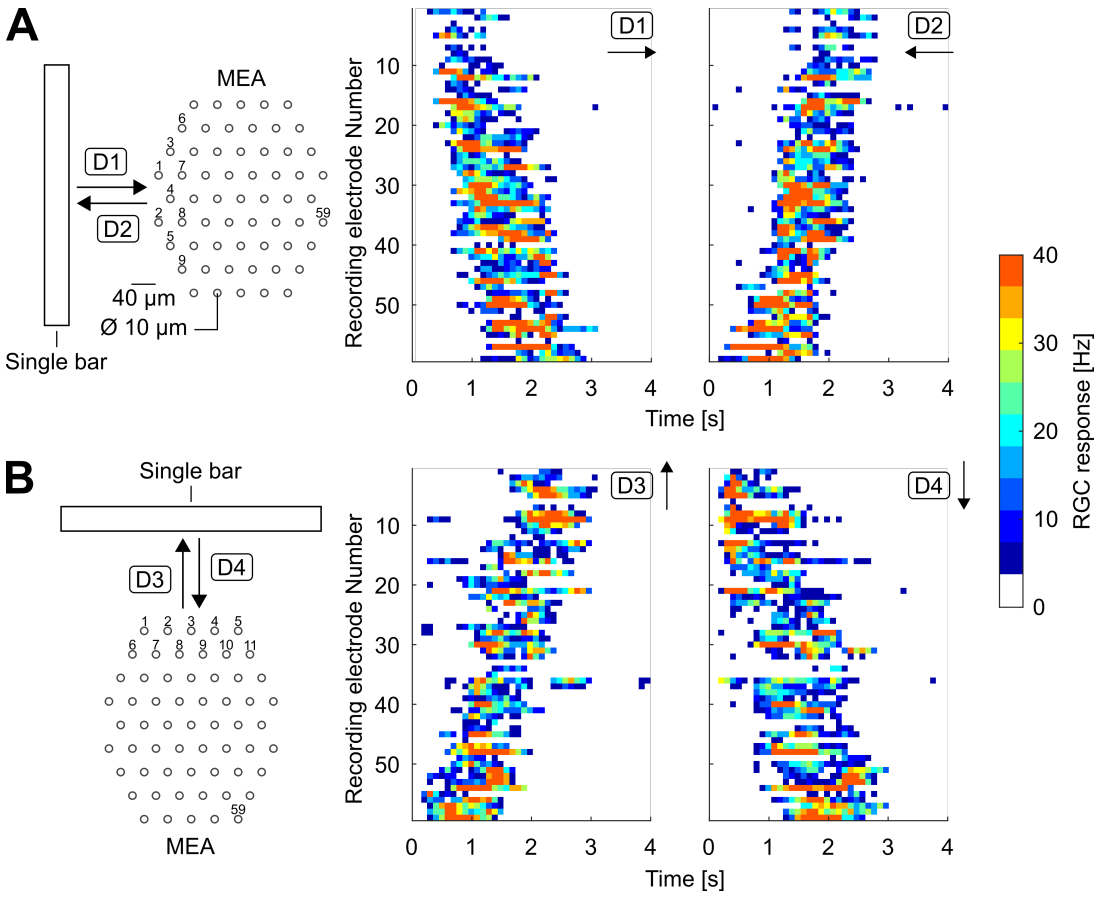

Figure 3.2: Light stimulation induced retinal ganglion cell responses to single bars moving in directions D1-D4. (A) Presentation of a light stimulation (L-stim) single bar moving in directions D1 and D2 with respective L-stim induced retinal ganglion cell (RGC) responses obtained at each electrode. Each electrode is indicated by a recording electrode number. (B) As in (A), but single bar movement in direction D3 and D4. Note the electrode numbers in parallel arrangement to the respective single bar orientation, for visualization purposes of the RGC response time course at each electrode. Retinal tissue not shown. Electrode diameter: 10 μm; Electrode spacing: 40 μm.

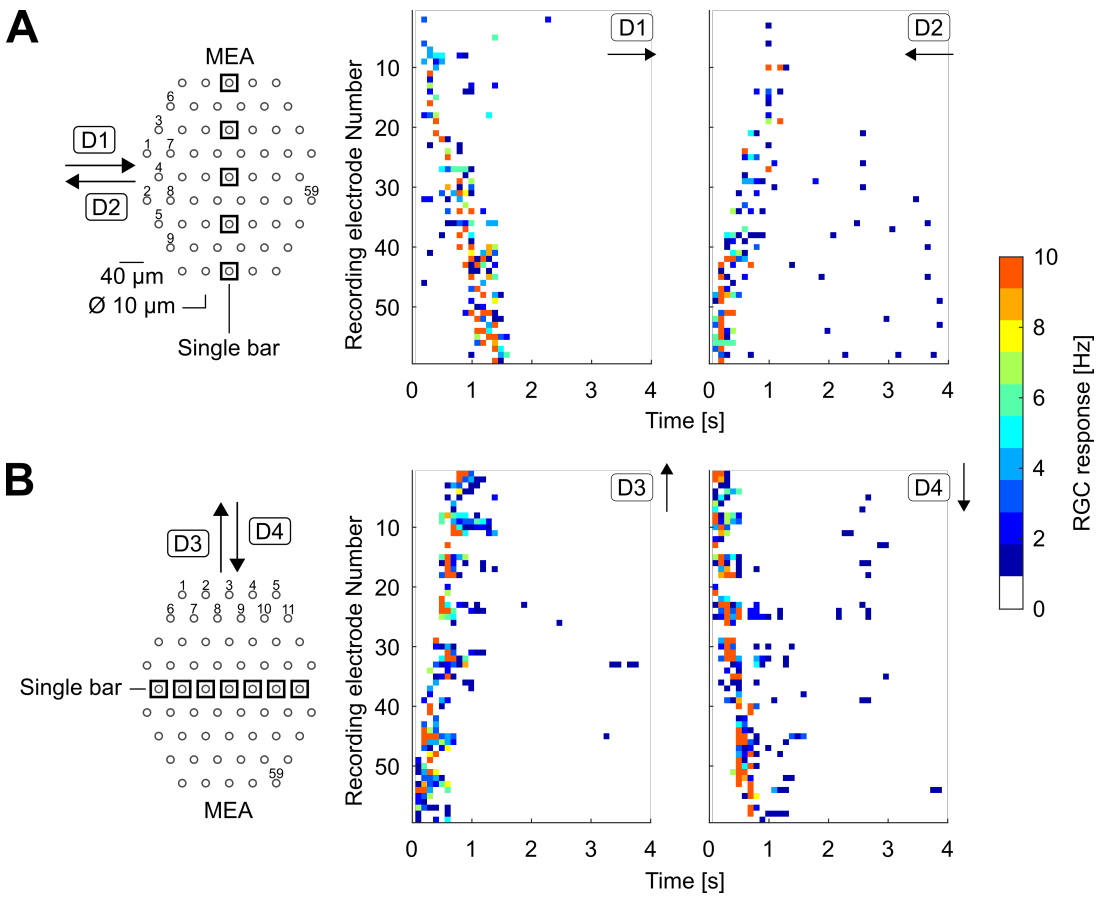

Figure 3.3: Electrical stimulation induced retinal ganglion cell responses to single bars moving in directions D1-D4. (A) Presentation of an electrical stimulation (E-stim) single bar moving in directions D1 and D2 with respective E-stim induced retinal ganglion cell (RGC) responses obtained at each electrode. Each electrode is indicated by a recording electrode number. (B) As in (A), but single bar movement in direction D3 and D4. Note the electrode numbers in parallel arrangement to the respective single bar orientation, for visualization purposes of the RGC response time course at each electrode. Retinal tissue not shown. Electrode diameter: 10 μm; Electrode spacing: 40 μm.

Spatial Spread of Responses limits Resolution of moving L-stim Bars and E-stim Bars

E-stim induced RGC signals show different response characteristics as compared to their L-stim induced counterparts. Figure 3.4 shows examples of RGC response patterns in dependence on different single bar and double bar stimulation patterns. Compared to L-stim, the spatial signal spread of the responses appears with higher proximity to the stimulus for E-stim. The responses spatially spread up to ~ 80 μm in E-stim single and double bars (Stett, 2000, 2007) (figure 3.4 A).

Time Course of Responses at Single Electrodes determine temporal Resolution of different L-stim Bars and E-stim Bars

Compared to the RGC responses of single bar stimulation, double bar induced RGC responses show two distinct peaks in all configurations (figure 3.4 B). E-stim induced RGC responses appear more local as compared to the L-stim induced responses. In L-stim bars, with BSspace = 240 μm at v = 220 $\mu m/s$, peaks of the fit are with 1.3 s wider apart as compared to the same BSspace at the faster velocity of v = 550 $\mu m/s$ with 0.6 s, without indication for temporal fusion of RGC responses. With BSspace = 40 μm, the peak-to-peak timings are 0.5 s for v = 220 $\mu m/s$ and 0.4 s for v = 550 $\mu m/s$. An indication for RGC response-fusion can be seen with BSspace = 40 μm at v = 220 $\mu m/s$ with a maximum peak-trough ratio of 34.9/13.5 (Hz) = 2.6. In contrast, E-stim induced responses with BSspace = 240 μm show a similar response pattern for both velocities, v = 220 and 550 $\mu m/s$ with peak-to-peak timings of 2.3 s and 1.7 s. At the smaller bar distance of BSspace = 40 μm the peaks are closer to each other with 0.9 s for v = 220 $\mu m/s$ and 0.4 s for v = 550 $\mu m/s$. In all shown cases of double bar stimulation, the second peak of the response is smaller than the first peak, and no fusion of peak responses was observed. In this context it should be mentioned that in such measurements with BSspace = 40 μm at v = 550 $\mu m/s$ two distinct peaks are not visible for all experimental trials (visible at ~ 30 % of electrodes for a recording-run), indicating

possible fusion of RGC responses. For a detailed investigation of the underlying mechanisms, further experiments would be required to obtain statistical measures.

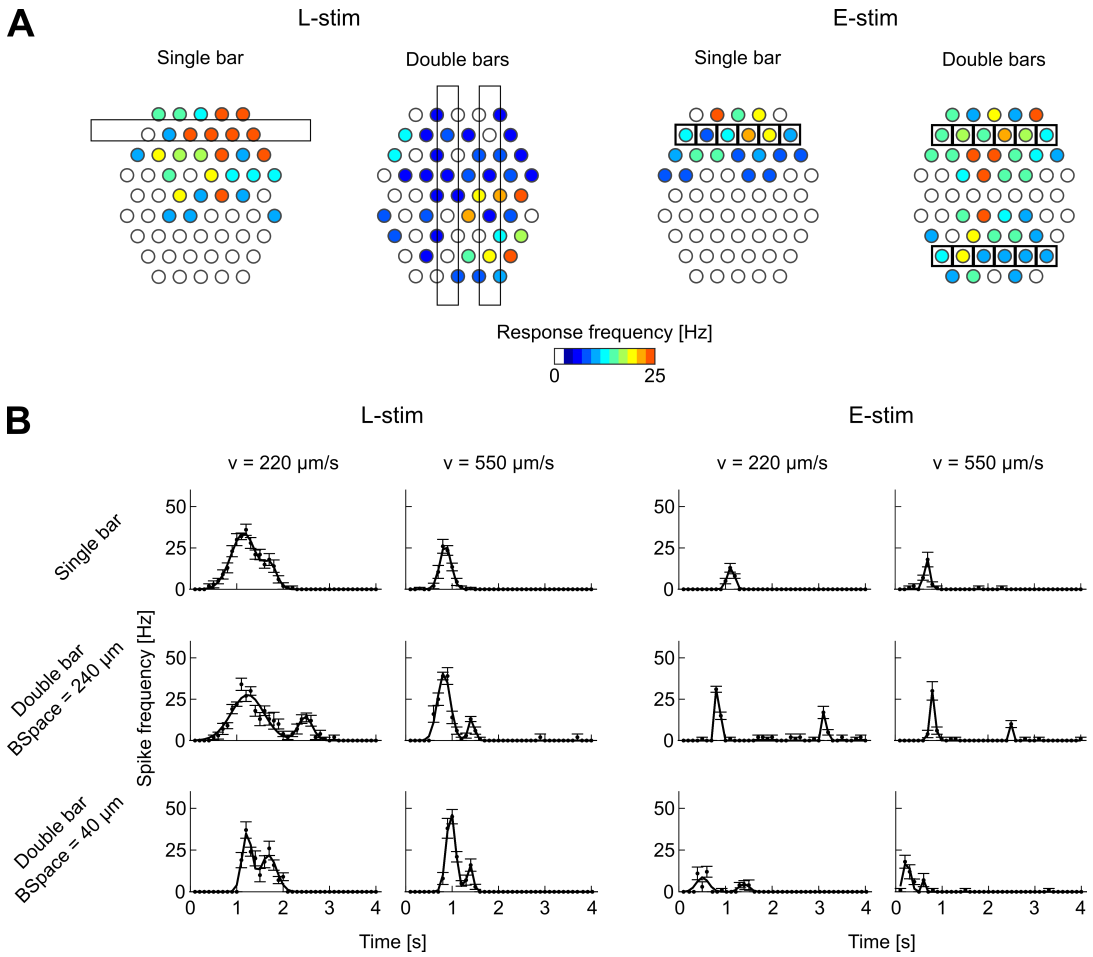

Figure 3.4: Retinal ganglion cell response patterns in dependence on single bar and double bar stimulation. (A) Light stimulation (L-stim) bars and electrical stimulation (E-stim) bars with respective stimulation induced retinal ganglion cell (RGC) responses obtained at each electrode, at sample time points; bold squares indicate stimulation electrodes for E-stim. Retinal tissue not shown. Note the spatial spread of RGC responses. Electrode diameter: 10 μm, shown schematically for visualization purposes; Electrode spacing in horizontal and vertical direction: 40 μm. (B) Examples of stimulation induced RGC responses at single electrodes for different L-stim patterns and E-stim patterns (Single bar, Bar spacing BSpace = 240 μm or 40 μm), moving at different velocities (v = 220 $\mu m/s$ or 550 $\mu m/s$). Line graph shows a gaussian fit (2-term gaussian fit for 2 distinct peaks). Error bars: ± SEM.

3.1.3 Direction Selective Activity

Direction selective index (DSI) values were calculated for different L-stim induced RGC responses and electrically induced RGC responses. The analysis yields an average number of recording electrodes with DSI > 0.6 of 5.9 ± 4.2 % for L-stim induced responses in a measurement. For electrically induced responses this value is 8.5 ± 3.4 %. Figure 3.5 shows examples of direction selective activity measured at single electrodes for both, L-stim induced moving-bar stimulation and electrically induced moving-bar stimulation. It can be observed that even though in cases of direction selectivity (DSI > 0.6) (see chapter 2.3, page 20), there is always a response when the stimulus moves in any of the other directions as well. This result supports the expositions in chapter 2.2.1, page 15. The almost uniform spacing of cells across the retina in a given mosaic (Roska, 2014) allows arbitrary retinal tissue orientation.

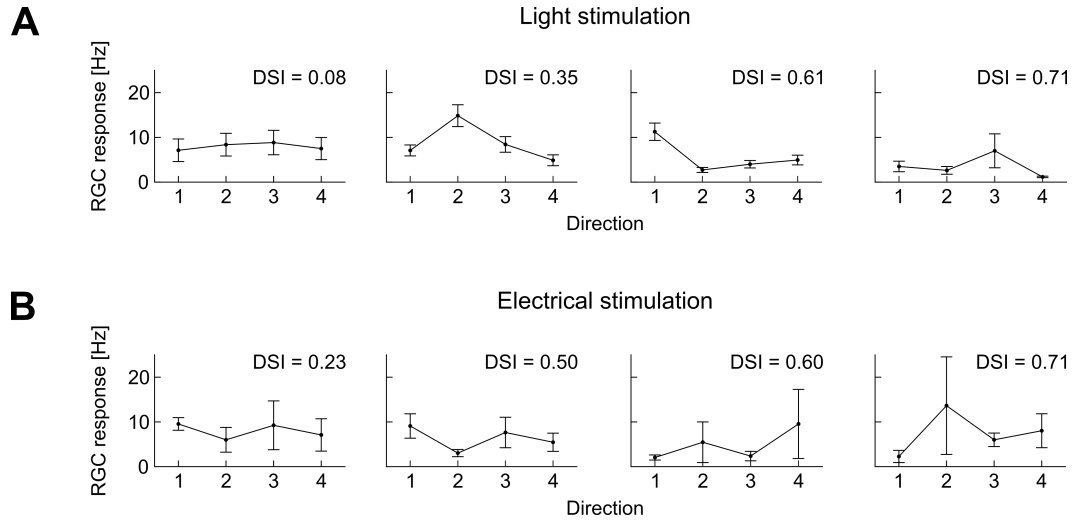

Figure 3.5: Direction selective activity measured at single electrodes. (A) Examples of tuning curves as mean retinal ganglion cell (RGC) responses in dependence on stimulus direction for light stimulation (L-stim) with a single bar moving at velocity v = 220 $\mu m/s$ with corresponding direction selective index (DSI) values. (B) As in (A), but for electrical stimulation (E-stim). Each tuning curve is taken from another recording electrode. Error bars: ± SEM.

3.1.4 Stimulus Anticipation indicated by Retinal Ganglion Cell Responses

L-stim induced RGC responses to moving-bar stimulation show the presence of RGC activity already before the stimulus reaches the respective recording location on the MEA. This is the case for both tested velocities of v = 220 $\mu m/s$ (figure 3.6 (A)) and 550 $\mu m/s$ (figure 3.7 (A)). In general, the observed motion anticipation mechanism is in agreement with Berry (1999). This effect was not observed for responses to electrically induced moving-bar stimulation (figure 3.6 (B), figure 3.7 (B)). For v = 220 $\mu m/s$, RGC responses were observed with proximity to the stimulus. For v = 550 $\mu m/s$ the responses occur mainly later in time, after the stimulus run ended (figure 3.7 (B)). This is already the case at timepoint t = 0.8 s.

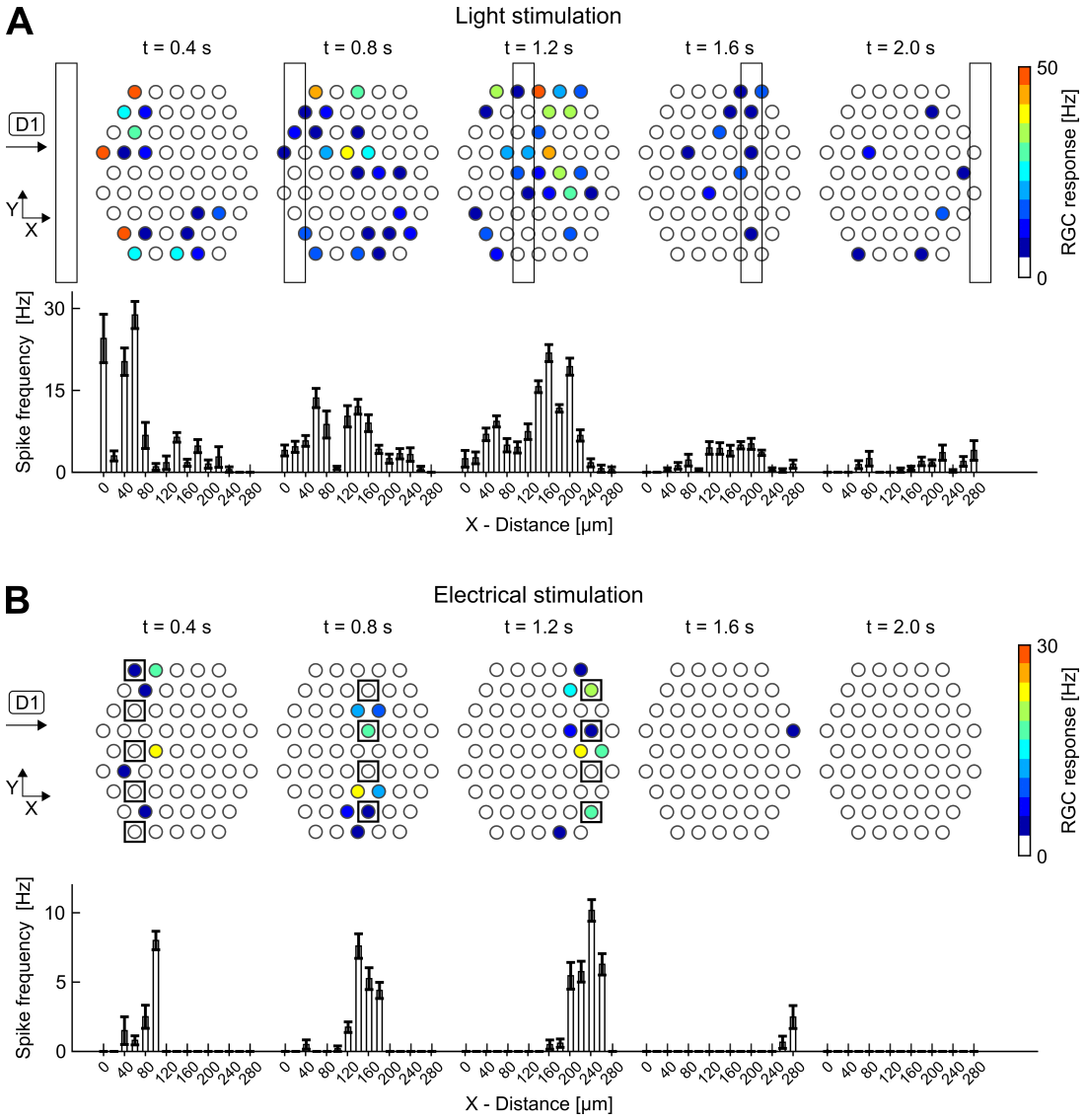

Figure 3.6: Anticipation of motion to stimuli moving at v = 220 $\mu m/s$. Moving-bar light stimulation (L-stim) across multielectrode array (MEA) recording field and corresponding extracellular retinal ganglion cell (RGC) responses at different locations. (A) Moving light bar stimulus along direction D1 at different timepoints and respective RGC responses recorded at different electrodes. Bar velocity v = 220 $\mu m/s$. Electrode diameter = 10 μm, schematically shown for visualization purposes. Bottom: Extracellular RGC responses averaged along orthogonal direction (y) to the bar motion to indicate RGC activity which occurs before the stimulus reaches the actual recording location. (B) As in (A), but for moving transverse electrical bar stimulation. Retinal tissue not shown. TBS = 0.1 s. Error bars = ± SEM.

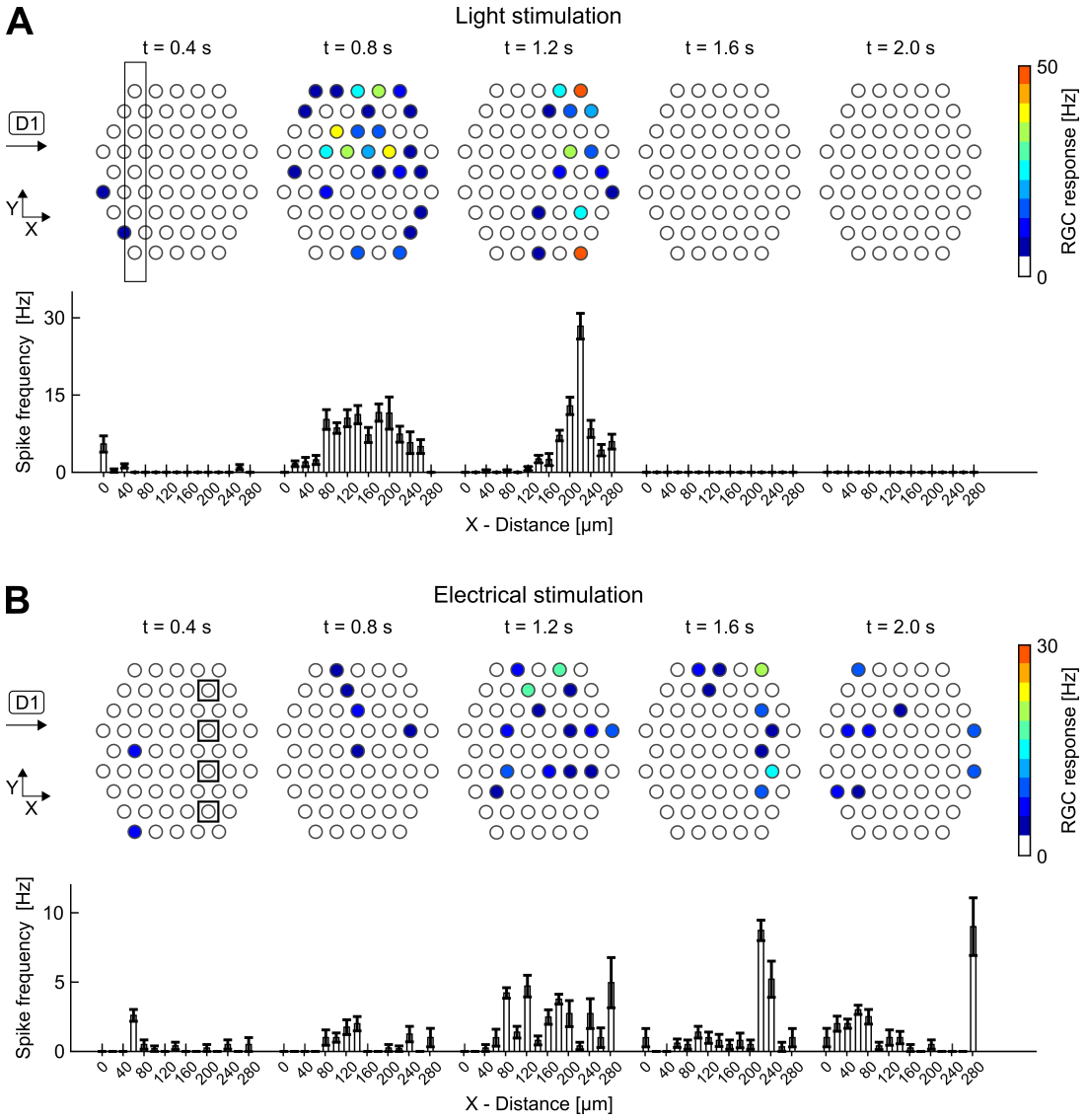

Figure 3.7: Anticipation of motion to stimuli moving at v = 550 $\mu m/s$. Moving-bar light stimulation (L-stim) across multielectrode array (MEA) recording field and corresponding extracellular retinal ganglion cell (RGC) responses at different locations. (A) Moving light bar stimulus along direction D1 at different timepoints and respective RGC signals recorded at different electrodes. Bar velocity v = 550 $\mu m/s$. Electrode diameter = 10 μm, schematically shown for visualization purposes. Bottom: Extracellular RGC responses averaged along orthogonal direction (y) to the bar motion to indicate RGC activity which occurs before the stimulus reaches the actual recording location. (B) As in (A), but for moving transverse electrical bar stimulation. Retinal tissue not shown. TBS = 0.1 s. Error bars = ± SEM.

3.2 Assessment of Electrically induced Retinal Ganglion Cell Responses

Light Stimulation induced Response Library for Training

Examples of L-stim induced RGC response sequences from the L-stim induced response library (LRL) are shown in figure 3.8. As expected, stimuli with faster velocities show a shorter RGC response time as compared to the ones with slower velocities. Example: RGC responses induced by single bars with D4, BSpace = 40 μm, v = 220 and 550 $\mu m/s$ yield an approximately two-fold shortening of the response time course for v = 550 $\mu m/s$ compared to v = 220 $\mu m/s$. Double bar stimuli with higher velocities appear comparable to each other (D4, v = 550 $\mu m/s$, BSpace = 40 and 240 μm). The numbering of electrodes was done as in figure 3.2 (B), figure 3.3 (B), figure 2.4 (A) respectively, to provide a uniform reference for the artificial neural networks (ANNs).

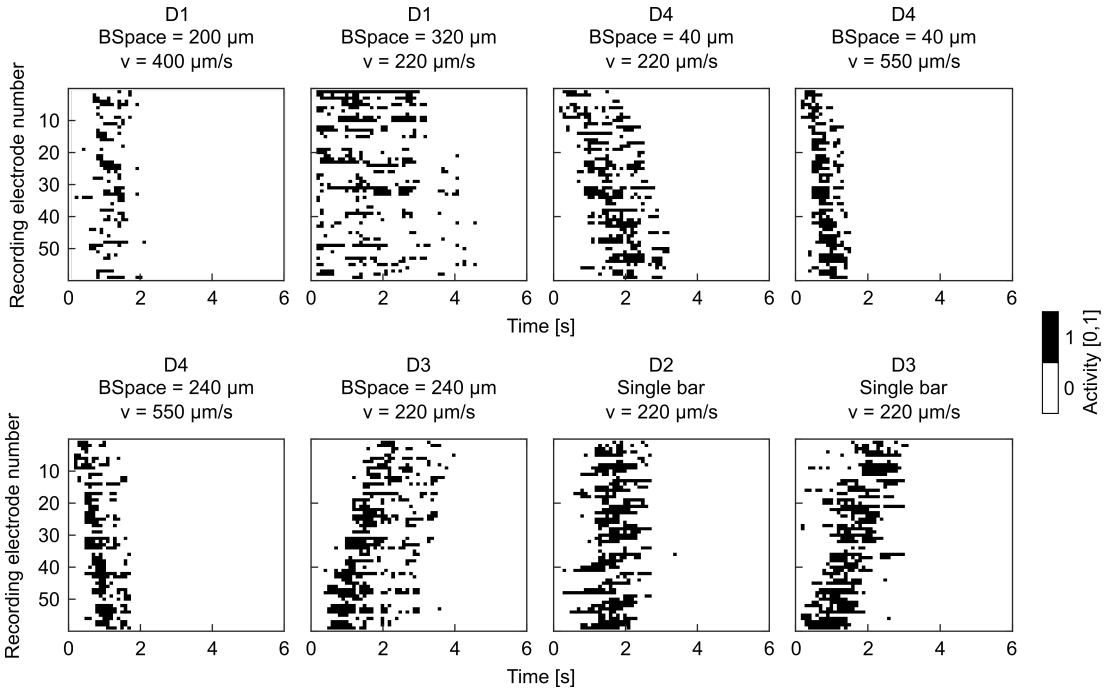

Figure 3.8: Examples of light stimulation induced single measurements. Each measurement shows binary retinal ganglion cell (RGC) responses as activity [0,1] for all recording electrodes over a recording duration of 6 s with a time bin size of TBS = 0.1 s. Electrode numbering as in figure 3.2 (B) and figure 3.3 (B). Obtained matrices are used as training and validation data for the artificial neural networks (ANNs).

Electrical Stimulation induced Response Library for Testing

Electrically induced single measurements were recorded to build an electrical stimulation (E-stim) induced response library (ERL) as a test dataset. This dataset was not used for training the ANNs. Figure 3.9 shows examples for E-stim induced measurements, sequences respectively. The numbering of electrodes was the same as for the LRL, so that the ERL classes can be compared to the LRL classes.

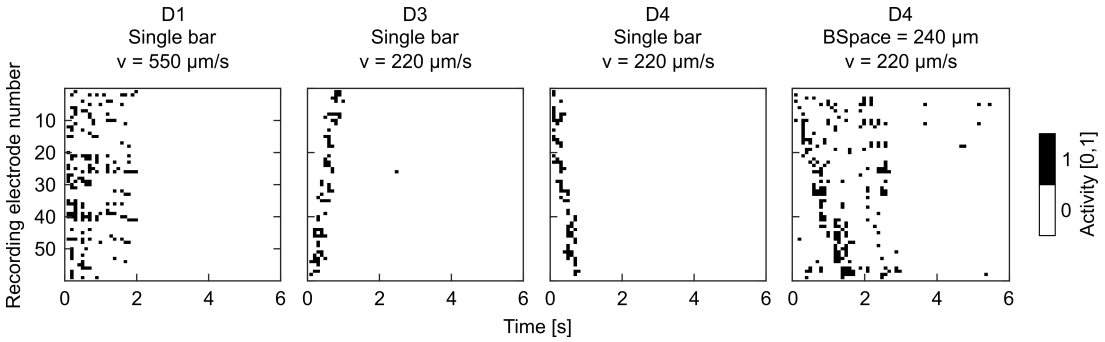

Figure 3.9: Examples of electrically induced single measurements. Each measurement shows binary retinal ganglion cell (RGC) responses as activity [0,1] for all recording electrodes over a recording duration of 6 s with a time bin size of TBS = 0.1 s. Electrode numbering as in figure 3.2 (B) and figure 3.3 (B). Obtained matrices are used as held out data for artificial neural network (ANN) testing.

3.2.1 Artificial Neural Network based Pre-Evaluation of Light Stimulation induced Responses

For TBS = 0.1 s, 31 ANN hidden layer neurons yield 1 % of misclassified samples. For TBS = 0.2 s the fraction is also 1 %, with 30 neurons. For TBS = 0.3, 0.5 and 0.7 s, the fraction of misclassified samples is 2 % with 42, 58 and 52 neurons respectively. 6 % of misclassified samples are given with 61 neurons for TBS = 1.0 s. The evaluated fraction of false classifications for different TBSs is shown in figure 3.10 (A). The fraction of false classification for all TBSs is shown in figure 3.10 (B) for a direct comparison.

Data from stimulus directions D5 to D8 were not considered in further analyses, since the MEA resolution was limited, considering a too high similarity between certain stimulus directions.

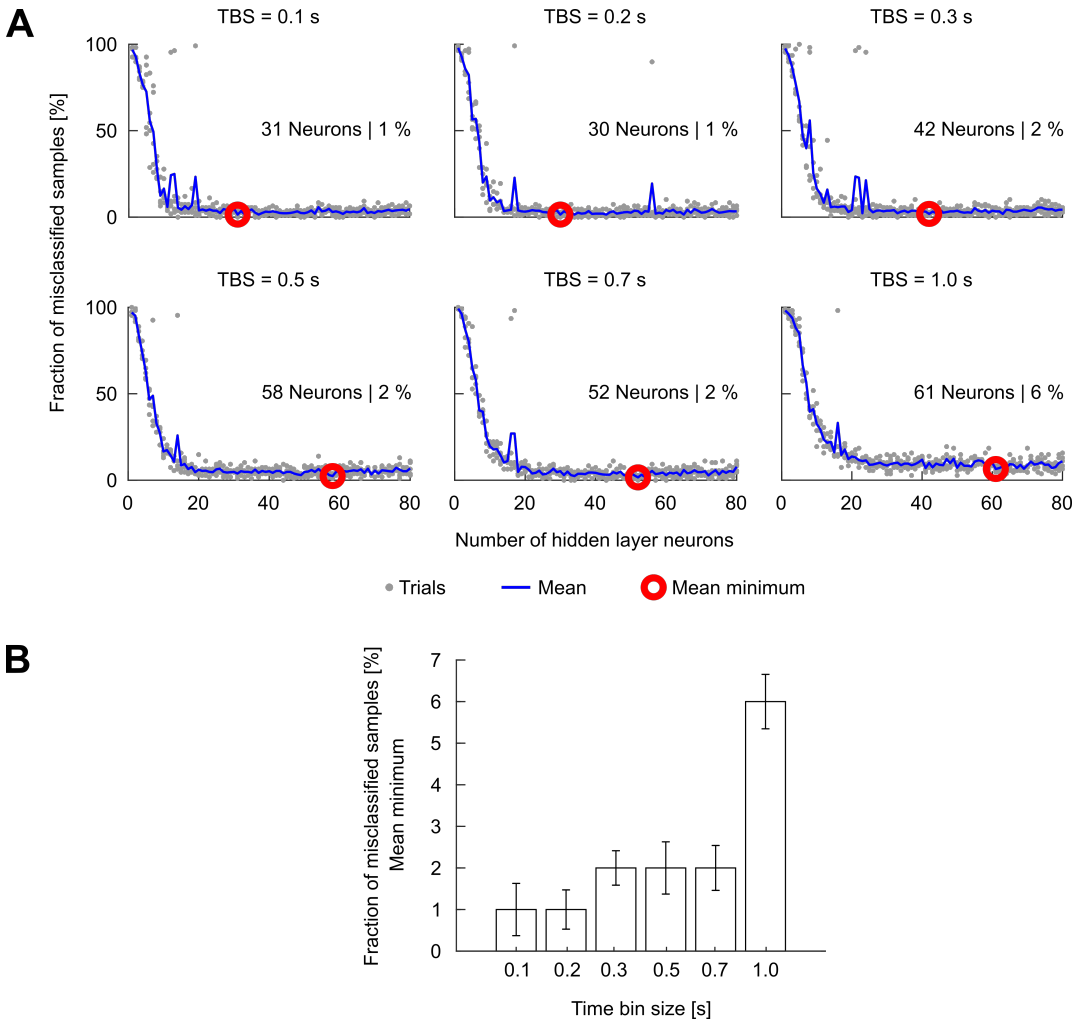

Figure 3.10: Fraction of false classifications varying time bin size and number of neurons in the hidden layer. A shallow artificial neural network (ANN) trained on 48 light stimulation (L-stim) response classes was used for estimation. (A) Fraction of misclassified samples for different numbers of neurons in the hidden layer. Insets show the number of neurons at the minimum fraction of misclassified samples. Example: For TBS = 0.5 s, 58 neurons yield 2 % of misclassified samples. (B) Fraction of misclassified samples for different time bin sizes (TBSs). Error bars: ± SEM.

3.2.2 Classification with Convolutional Neural Networks

Regarding the uniform retinal tissue properties mentioned in chapter 2.2.1 and the results from chapter 3.1.3, in this approach one could neglect different stimulus directions in the classification and only focus on stimulus velocity, single bars and bars with different bar spacings. Nevertheless, four stimulus directions were considered in this approach to account for differences between directions D1+D2 and D3+D4 based on the MEA layout. D1 and D2 use the same electrode arrangement. D3 and D4 use a more dense electrode arrangement.

CNN Features

The features learned by the convolutional neural networks (CNNs) during training with the LRL are visualized through MATLAB's function deepDreamImage (TMW), visualizing the features as high resolution images that strongly activate respective channels of the network. Figure 3.11 shows learned features of a CNN trained with 104 L-stim induced response classes. Figure 3.11 (A) shows the features of convolutional layer 1, with a relatively low complexity; filters: 4 x [3 3]. The first eight features of the fully connected layer are shown in figure 3.11 (B). Here the typical structures of the recording sequences are recognizable (compare figure 3.8). Also in figure 3.11 (C), these structures are visible in the features of the softmax layer. See LeCun (2015) for a methodological review.

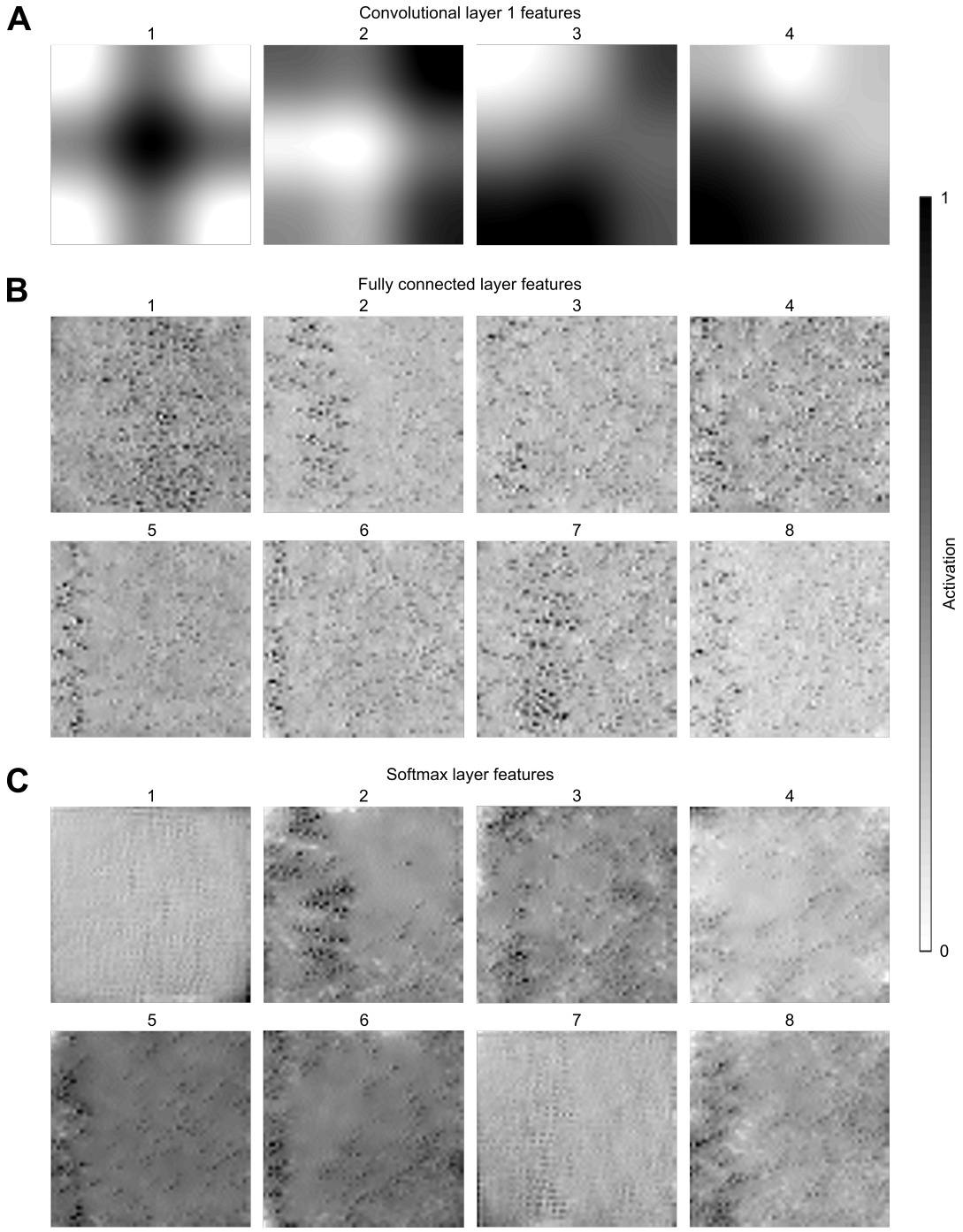

Figure 3.11: Convolutional neural network features. Convolutional neural network (CNN) features learned during training with the light stimulation induced response library (LRL). Each feature is visualized as a high resolution image that strongly activates the respective channel of the network through MATLAB's function deepDreamImage. (A) Features of convolutional layer 1 with a relatively low complexity, for convolutional layer filters: 4 x [3 3]. (B) First eight features of the fully connected layer out of a maximum of 104, showing typical structures of the recording sequences (C) First eight features of the softmax layer out of a maximum of 104, also indicating the structures of the recorded sequences.

In figure 3.12 (B), a confusion matrix is shown for training and testing with four classes. Each matrix element shows the fraction of classified samples as the predicted class. Diagonal elements indicate the true positive (TP) classifications (true positive rate = sensitivity) which correspond to target class = predicted class.

Note: A class contains single / double bars with Bspace + direction + velocity. A Set contains a group of certain defined classes.

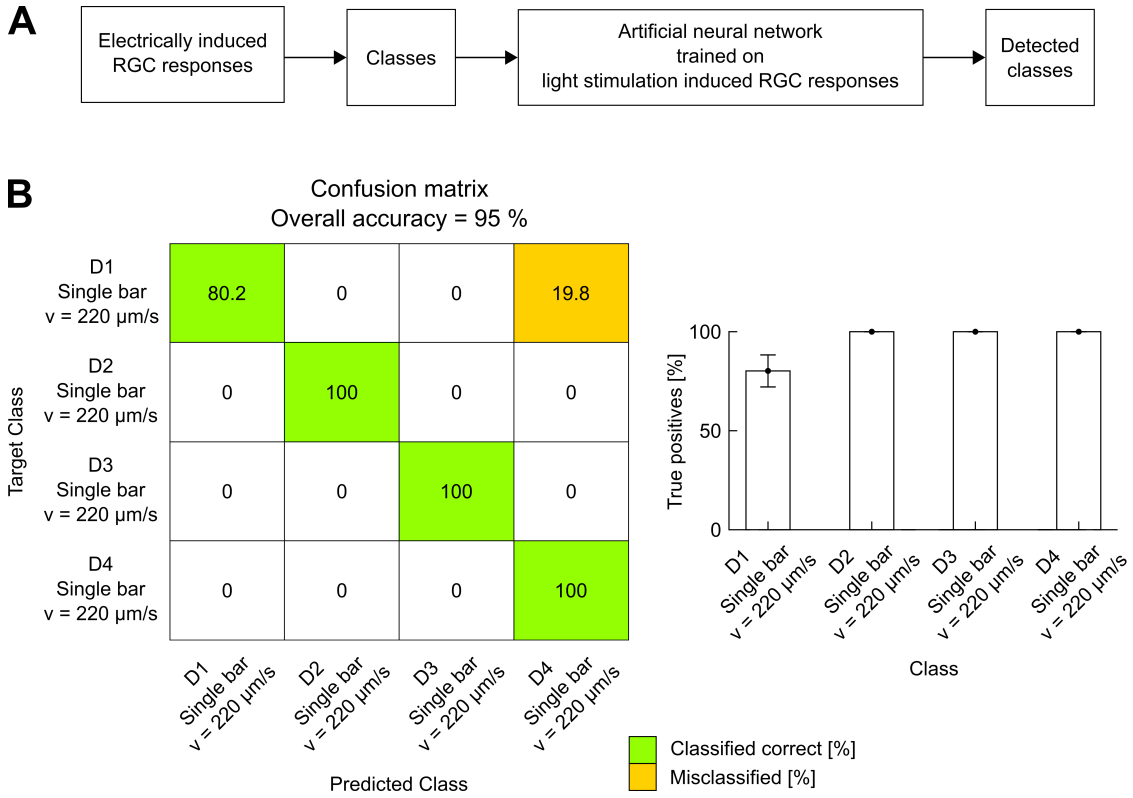

Figure 3.12: Example classification scheme. (A) Schematic of the classification procedure. (B) Example classification performance visualized through a confusion matrix for training and testing with four classes (See figure 3.15, training with light stimulation induced responses and testing with electrically induced responses with Set 3). Rows indicate the target class, the real class respectively. Columns indicate the predicted class. Each position in the matrix shows the fraction of classified samples as the predicted class. Elements on the diagonal indicate the true positive (TP) classification (true positive rate = sensitivity) which corresponds to target class = predicted class, with ideally 100 %. Target class D1, Single bar, v = 220 $\mu m/s$ was predicted correctly for 80.2 % of the samples whereas 19.2 % of this class were wrongly classified as D4, Single bar, v = 220 $\mu m/s$. All other classes were classified correclty with 100 %. (B) Fraction of true positives for the matrix in (A). Error bars: ± SEM.

Classification of classes from the ERL using a CNN trained with a LRL supports result-based decisions as described below:

1. Testing the whole 24-class (Set 1) ERL with the CNN trained on the whole LRL yields an overall accuracy of 20.6 %. Six electrically induced response classes (Set 8) were correctly classified by the network. These classes are single bars with directions D1 - D4 and v = 220 $\mu m/s$ and double bars with directions D3 and D4 with Bspace = 240 μm and v = 220 $\mu m/s$. The classification of 24 electrically induced response classes is represented in figure 3.13.

2. Exclusively testing the six correctly classified classes (Set 8) shown in figure 3.13 (B) with the same 104-class trained L-stim induced response network, the overall accuracy is 95.6 %, since remaining test classes which were not detected in the previous step were not used (figure 3.14). An overview of the class configurations used for training and testing is represented in figure 3.15 (A).

3. Reducing Sets to form other Sets as well as merging of different Sets was performed based on intermediate results and similarities between classes: Only classes with same directions and velocities were merged together for testing purposes. Figure 3.15 (B) shows the overall accuracies for different train-test-combinations. Training and testing with the respective classes according to Set 3 yields an accuracy of 95.0 %. Training with Set 1 and testing with Set 3 yields an 80 % accuracy.

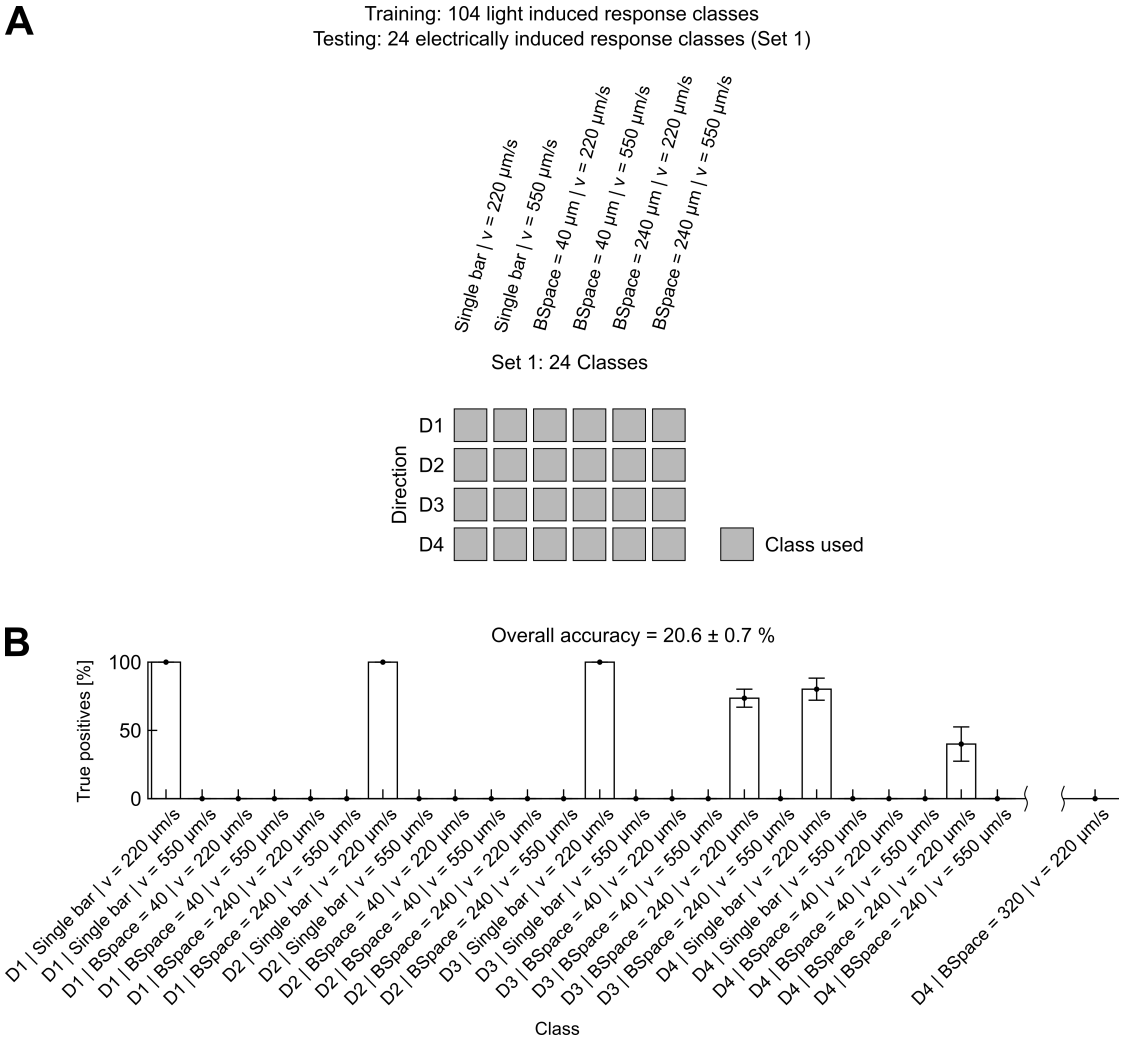

Figure 3.13: Classification of 24 electrically induced response classes. A convolutional neural network (CNN) was trained with 104 light stimulation (L-stim) induced response classes. The network was then tested with 24 electrically induced response classes. (A) Schematic of the classes in the test dataset with different directions for the moving-bar stimulation (D1 - D4), single bars and double bars with different bar spacing (BSpace = 40 μm or 240 μm) and different velocities (v = 220 $\mu m/s$ or 550 $\mu m/s$). (B) Fraction of true positives for the electrically induced response classes tested with the CNN trained on 104 L-stim induced response classes (class number 104 = D4, Bspace = 320 μm, v = 220 $\mu m/s$ indicated on the abscissa). Six classes were correctly classified by the network, indicated by the true positives [%]. Detected classes are single bars, D1 - D4 with v = 220 $\mu m/s$ and double bars, D3 and D4 with Bspace = 240 μm and v = 220 $\mu m/s$. The overall accuracy is 20.6 %. Error bars: ± SEM.

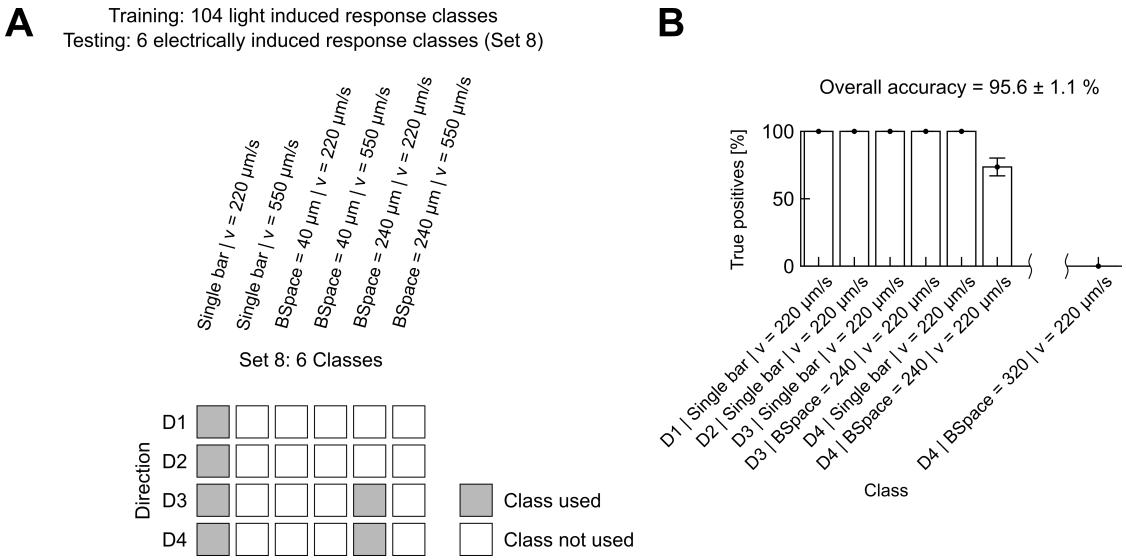

Figure 3.14: Classification of six electrically induced response classes. The same convolutional neural network (CNN) as used in figure 3.13 was used (trained with 104 light stimulation (L-stim) induced response classes). The network was tested with the six electrically induced response classes which were correctly classified within the whole 24-class electrical stimulation (E-stim) induced response classes (figure 3.13). (A) Schematic of the classes in the test dataset consisting of single bars, D1 - D4 with velocity v = 220 $\mu m/s$ and double bars, D3 and D4 with bar spacing Bspace = 240 μm and v = 220 $\mu m/s$, defined as Set 8. (B) Fraction of true positives for the electrically induced response classes tested with the CNN trained on 104 L-stim induced response classes (class number 104 = D4, Bspace = 320 μm, v = 220 $\mu m/s$ indicated on the abscissa). Testing with exclusively these six classes yields an overall accuracy of 95.6 %. Error bars: ± SEM.

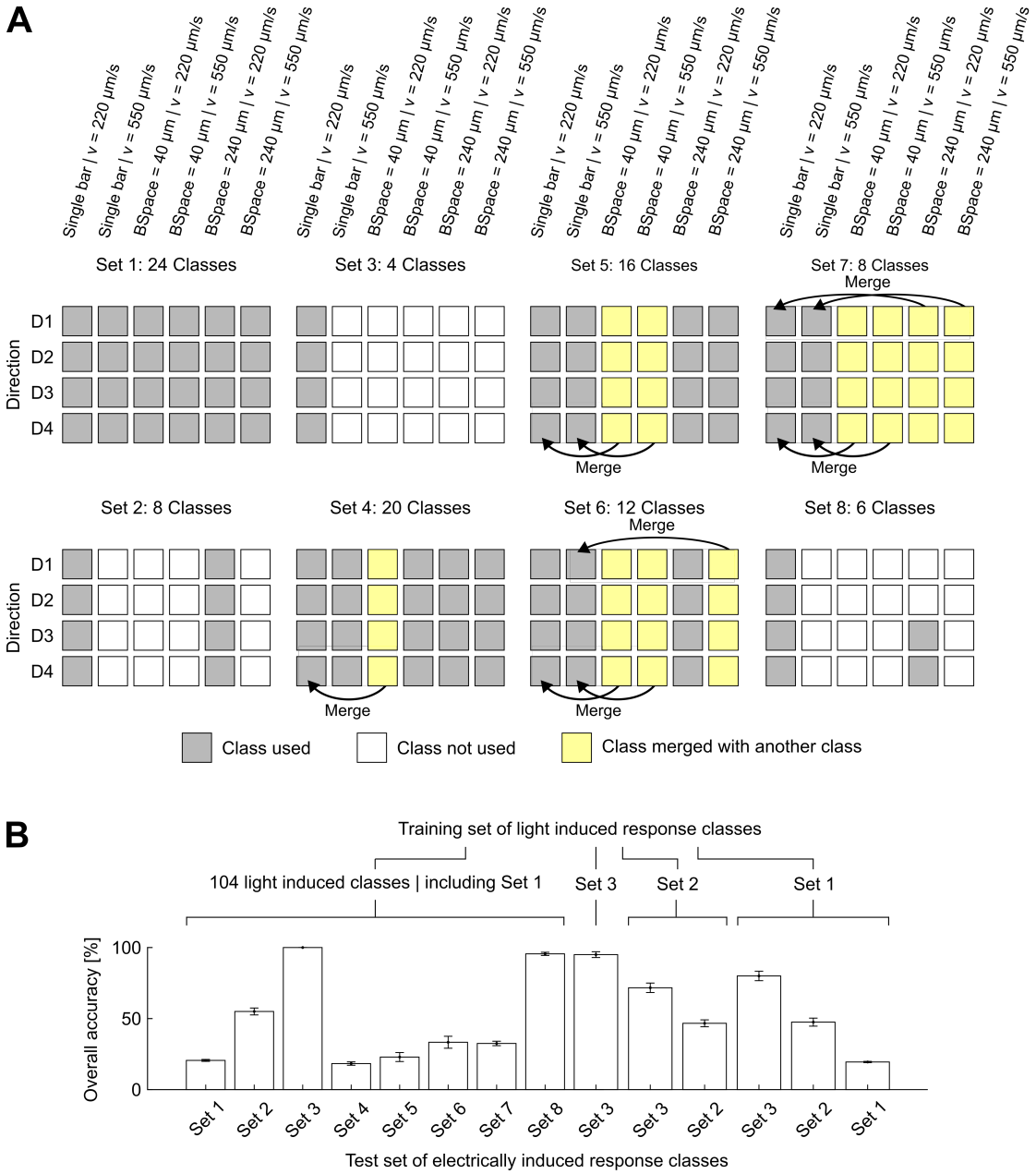

Figure 3.15: Constellations of different classes defined as Sets. (A) Different constellations of classes. Set 1: 24 classes, representing the whole dataset of electrically induced response classes. Set 2, Set 3 and Set 8 consist of respective classes of Set 1. In Set 4 to Set 7 certain classes were merged together. The light stimulation induced response library (LRL) with all 104 classes is not shown because of space limitations for visualization. (B) Overall accuracies for different train-test constellations. Different Sets were used for training and testing. Example: Training a convolutional neural network (CNN) according to Set 1 with 24 light stimulation (L-stim) induced response classes and testing the network with the four electrical stimulation (E-stim) induced response classes according to Set 3 yields an overall accuracy of 80 % (third bar from right side). Error bars: ± SEM.

3.2.3 Electrical Stimulation Patterns for the Application in Retinal Implants

As a practical example of how the preceding ANN based testing framework can be used, this section describes E-stim patterns to counteract fading effects. This section is based on a method adapted from the work of Sunetra Basavaraju ((Basavaraju, 2018), Basavaraju S, Speck A, et al., in preparation). For the present work, this project is intended to give a brief overview of an example on how the ANN based testing framework can be used to support the selection of patterns for E-stim. Previous chapters deccribe RGC response characteristics based on different L-stim and E-stim patterns. Based on the spatial response characteristics of electrically induced responses together with the ANN based evaluation, a suitable bar spacing (BSpace) for the separation of two electrically induced bars can be defined based on the preceding elaborations.

Visual responses perceived through retinal implants seem to fade away quickly with repeated E-stim (Fornos, 2012; Stingl, 2013, 2015; Hafed, 2016). In retinal implant vision, E-stim is traditionally presented through all the activated electrodes at once. E-stim of this accordance is happening repeatedly, thus a reduction of responses is seen after a short period of time (seconds), resulting in fading of visual perception. To avoid repeatedly stimulating the same retinal regions and also to maintain visual sensations, this approach proposes to break down the conventional E-stim method into spatio-temporal E-stim patterns. Based on the results of the testing framework, E-stim single bars (D1 - D4) and double bars with BSpace = 240 μm (D3 or D4), both at a moderate velocity of v = 220 $\mu m/s$ could be used. Because in this step, there is no directional stimulus motion involved, we considered the relatively sparse electrode activation used in E-stim of D1 and D2 as suitable orientation on the MEA layout. A double bar object with BSpace = 160 μm was defined using 5 electrodes for each bar (figure 3.16 (A)). As a control measure, the E-stim object was presented in a conventional way by repeatedly producing electrical pulses. This was performed for a period of 90 s,

simultaneously stimulating all the electrodes to demonstrate the effect of fading, with the pattern called BarSimul (figure 3.16 (B)). To overcome this effect, the object was presented using the ”alternating electrode pattern” at different frequencies for a period of 90 s, with the pattern called BarAltern (figure 3.16 (A) and (C)). It was observed that a rapid decrease in responses occurred due to ”stationary” double bar object stimulation, which is seen already at recording timepoint t = 10 s. With ”alternating electrode pattern” stimulation for the double bar object, the responses were consistent for 90 s even at 10 Hz E-stim frequency. Although being more sparse, responses at t = 90 s were also visible at the stimulus locations for an E-stim frequency of 20 Hz. No fusion of responses evoked by E-stim at the two bar positions (grey shaded bars) was observed. See figure 3.16 (C).

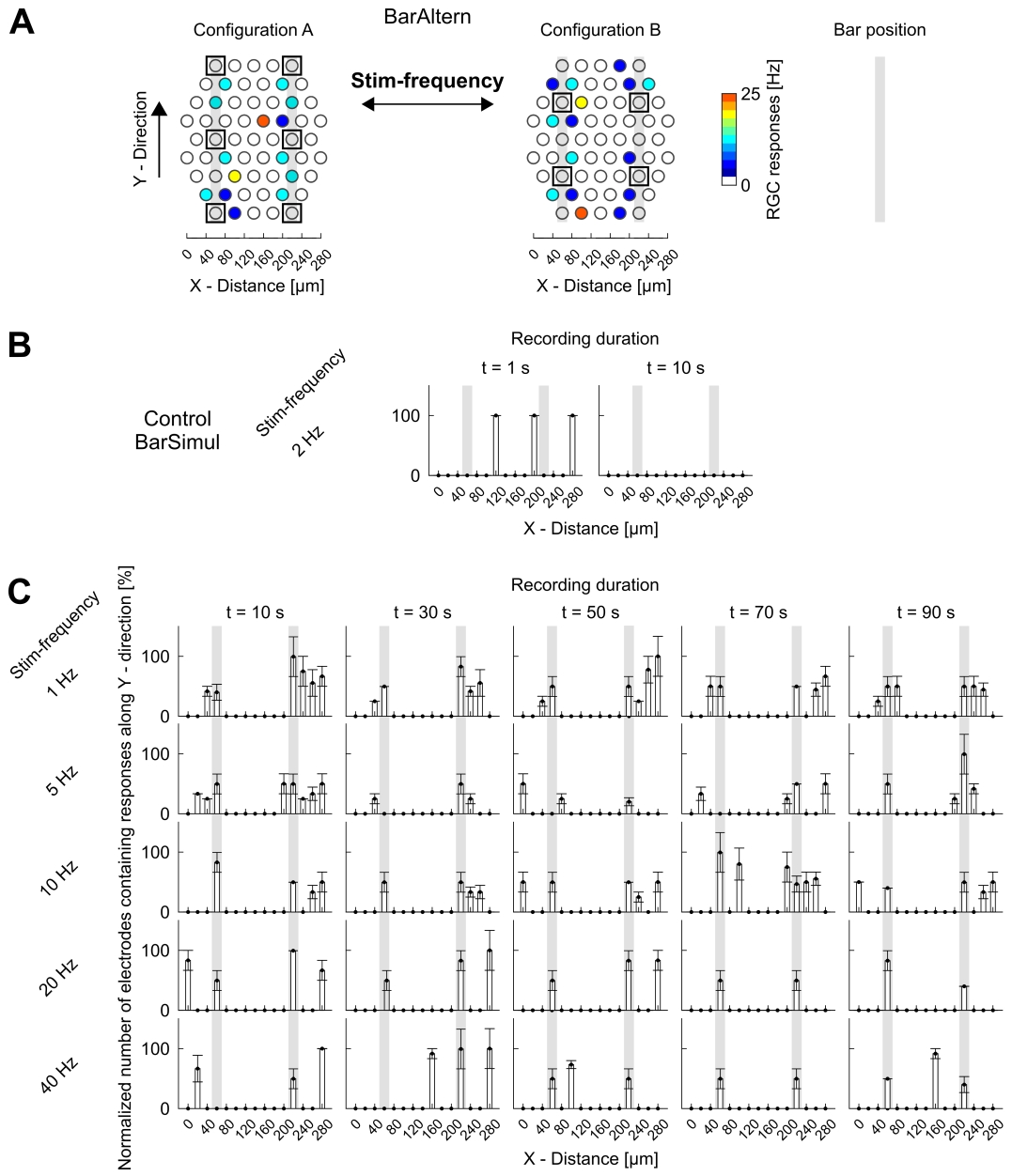

Figure 3.16: Alternating electrical stimulation of double bars. (A) Electrical stimulation (E-stim) bars with respective stimulation induced retinal ganglion cell (RGC) response obtained at each electrode, at sample time points; bold squares indicate E-stim electrodes. Configuration 1 and Configuration 2 are stimulated alternatingly with the pattern BarAltern. Electrode diameter: 10 μm, shown schematically for visualization purposes; Electrode spacing in horizontal and vertical direction: 40 μm. (B) E-stim, using a simultaneous activation of the stimulation electrodes with the stimulation principle BarSimul, as a control measure. Stimulus locations are indicated by grey shaded bars. Panels show the normalized number of electrodes containing responses along Y - direction at the respective X - distances when stimulating with the BarSimul principle. 0 μm mark represents the first column of MEA electrodes from the left. Each panel represents a sample time point. (C) as in (B), but for the BarAltern pattern explained in (A). E-stim at -1 V, pulse width = 0.5 ms, impedance ~ 0.7 MOhm. Error bars: ± SEM.

Chapter 4

Discussion & Conclusions

In this chapter, stimulus-dependent retinal ganglion cell (RGC) responses and the artificial neural network (ANN) based analysis for the assessment of electrical stimulation (E-stim) induced RGC responses are discussed. Stimulation induced RGC responses are described with special attention on E-stim patterns. Further, the ANN based object discrimination is shown, closing with the conclusion in the last part.

4.1 Retinal Ganglion Cell Responses

RGC response characteristics were analyzed on the basis of different response features to investigate and understand plausible input parameters for E-stim of retinal tissue. In the first part, spatial spread characteristics of E-stim induced RGC responses are discussed. In the second part, direction selective activity induced by L-stim and E-stim is described. Moving stimulus prediction indicated by RGC responses is considered in part 3.

4.1.1 Spatial & Temporal Properties of Retinal Ganglion Cell Responses

Spatial spread of stimulation induced responses can in general hinder discriminative analyses when driving towards resolution limits. Considering one degree of visual angle corresponding to 31 μm in the mouse retina (Remtulla, 1985) and a visual acuity of the mouse with 0.5 cycles/degree (Prusky, 2000), it was possible to induce RGC responses in relatively local regions. At a stimulation strength of -1000 mV we found a spatial spread of the responses up to 80 μm with responses decreasing with increasing distance. See figure 3.4 (A). This outcome was in agreement with previous E-stim studies (Stett, 2000, 2007; Haq, 2018).

Interestingly, E-stim induced response peaks (figure 3.4 (B)) are wider apart as compared to their L-stim induced pendants, which indicates a response delay higher than in L-stim induced responses, regarding the second response peaks. These results might appear logic. Nevertheless, the underlying mechanisms leading to such RGC responses are based on rather complex retinal computations such as gap-junctionally coupled networks of AII amacrine cells and RGCs (for review see (Kolb, 1994; Gollisch, 2010)). Interestingly, response shapes for L-stim induced RGC responses at v = 550 $\mu m/s$ for BSspace = 40 μm and 240 μm appear similar with peak-to-peak timings of 0.4 s and 0.6 s. Another remarkable

observation is the similarity of the peak-to-peak timing of E-stim induced RGC responses for BSspace = 240 μm at v = 220 and 550 $\mu m/s$ with 2.3 s and 1.7 s. This might be caused by spatial spread characteristics of E-stim induced RGC responses, influencing retinal regions already before the moving E-stim bar reaches the location of interest (see figure 3.4 (A) and chapter 3.1.2; further see (Stett, 2000, 2007; Haq, 2018)). The fact that the second peaks of the responses are smaller than the first peaks could be an indication for inhibition that is caused by the stimulation of the first bars of the double bar moving stimuli, based on receptive fields of RGCs (Example for a receptive field size: Roughly 300 μm; for review see (Berry, 1999; Fried, 2002; Johnson, 2018); for E-stim related receptive fields see Stutzki (2016)). The observed response features induced by double bar L-stim and E-stim are likely caused by center-surround mechanisms (Kuffler, 1953; Demb, 2015), with differences in intensity causing antagonistic surrounds in the inner retina through crossover inhibition ((Werblin, 2010), flashed light bar), and further mechanisms such as feedforward inhibition (for review see Johnson (2018)).

The observed prediction mechanisms (Berry, 1999) for moving L-stim bars further support the broader RGC response time courses induced by L-stim, when compared to E-stim. The fact that E-stim induced responses do not last as long as L-stim induced responses (figure 3.2 and 3.3) could be caused by inhibitory influences caused by E-stim, because the responses spread to respective locations before the stimulus reaches the actual location.

The experiments were performed with epiretinal E-stim, with a focus on the input-output relation rather than investigating detailed mechanisms of direct or indirect activation (for terms see Boinagrov (2014)). For a more detailed investigation regarding the underlying mechanisms such as inhibitory mechanisms, the used stimulation paradigm could be compared to subretinal E-stim, using a regime that allows such comparisons. There is a compromise between the general RGC response level and the spatial spread one has to consider. The stimulation

strength for E-stim used in this work with -1000 mV and 0.5 ms pulse width at an average impedance of 0.7 MOhm can be considered low (in accordance with Haq (2018)).

4.1.2 Independence of Stimulus Direction

With the almost uniform spacing of cells and cell type distribution across the retina in a given mosaic (Roska, 2014), direction selective activity was analyzed to understand the influence of direction selectivity for the downstream analyses. Direction selective activity was analyzed based on L-stim induced responses and E-stim induced responses to moving-bars. Calculating such values for electrically induced responses may be an unconventional approach which may not be accurately comparable to direction selectivity metrics, traditionally based on L-stim induced responses. Nevertheless it was observed that with a simple direction selectivity metric (Elstrott, 2008; Mazurek, 2014) it was possible to obtain a fraction of recording electrodes which indicate direction selective activity. One should consider the fact that the resolution of the electrical moving-bar stimulus is discrete, with the possible resolution limited by the MEA layout. The spatial spread of RGC responses across the retina also should not be neglected. As mentioned in chapter 4.1.1, the experiments were performed with epiretinal stimulation. Insights on plausible mechanisms should be analyzed based on experiments tailored to such a research question, also including subretinal stimulation.

Even though there are recording electrodes which indicate direction selevtive RGC activity, RGC activity was also observed in response to any of the other stimulus directions. In the further analyses the whole population information was used, which supported the recording procedure in a practical way, even considering the possible and likely presence of direction selective RGCs. Direction selectivity did therefore not play an important role in this work. Further, direction selective

RGCs were not found in primates (Euler, 2016; Schaeffel, 2017b). Building the assessment framework of E-stim induced responses directly on responses from the retinal read out, direction selective activity mechanisms were not investigated in detail. This aspect should particularly be considered when using retinal tissue samples from other species, with other cell topographies.

4.1.3 Retinal Stimulus Anticipation

As for the analysis of direction selective activity, motion anticipation mechanisms were not of interest in particular, since the assessment of E-stim induced responses was solely based on the retinal read out. L-stim induced responses to moving-bar stimulation show RGC activity already before the stimulus reaches the respective recording location on the MEA. The princpiple motion anticipation mechanism is in agreement with Berry (1999). Further, a required feature for motion anticipation is amacrine cell feedforward inhibition to RGCs (Johnston, 2015). The effect was not observed for responses to electrically induced moving-bar stimulation, indicating another shortcoming of E-stim when comparing it to natural mechanisms, together with other aspects such as observed differences in the spatial spread of responses and different time courses of responses. Like in the analysis of direction selective activity, one has to take into account that the underlying mechanisms and response characteristics of L-stim and E-stim are not comparable in a one to one fashion. Especially the MEA resolution as a fixed limitation is a component of great imortance when building conclusions. Deriving detailed recommendations for E-stim related motion anticipation based on the present analysis would be too vague. A more detailed and more explaining investigation of E-stim induced motion anticipation would be required to obtain more accurate numbers. This would require an even finer adjustment of E-stim and L-stim intensities for the close approximation of E-stim induced responses to L-stim induced responses. In such conditions, the testing framework as proof of concept could be of great use.

4.2 Object Discrimination

In this section, the artificial neural network (ANN) based object discrimination is discussed. In part 1, the classification of RGC response patterns is described, followed by L-stim patterns as a reference for training ANNs in part 2. The plausibility of the employed approach is examined in part 3, followed by descriptions on modifications and extensions of the introduced method and the implications for the development of electrical retinal implants in part 4 and part 5.

4.2.1 Classification of Retinal Ganglion Cell Response Patterns

E-stim induced responses were compared to L-stim induced responses, employing ANN models. The variance in retinal tissues and measurements was accounted for through the ANN based evaluation. A data based testing framework was created to estimate the retinal outcome as an early assessment to identify whether the retina has seen the respective L-stim induced objects or not. A black-box approach on the meta-level was applied, where all recorded RGC signals are considered. This work is not intended to build a new standard for the assessment of electrically induced responses or even a replacement of clinical trials. The framework can rather be understood as a supportive method, as an additional, robust guidance for early trials.

The shallow ANN architecture used for pre-evaluation (chapter 2.4.1) yielded solid results (see Warland (1997), where also a shallow ANN architecture was used, to decode spike trains). The pre-evaluation of L-stim induced RGC responses indicates that the obtained RGC responses could possibly be coded with a surplus of information, with respect to temporal resolution. This supports the assumption that temporally redundant signal content in the RGC responses occurs at least to a certain degree (see (Puchalla, 2005; Marre, 2015)).

Through the use of CNNs for the evaluation of E-stim induced responses, it was possible to isolate the parameter space for E-stim to a basic stimulus Set. In particular, the acutal results of the classification indicate that a narrowed down stimulation Set of six E-stim classes could be considered for sensible E-stim of mouse retinal tissues.

Given the nature of the approach, experimental iterations are required to design new E-stim paradigms, whereas fast tests are possible even without iterations. The choice of treating RGC responses as binary events in the classification process led to solid classifications. For future experiments, RGC response frequencies could be used for classification. This should be performed with a higher number of recording samples, to avoid possibly biased representations based on spatially local RGC response frequencies from underrepresented classes.

With the help of such a framework, new stimulation strategies could already be narrowed down to a limited parameter space, helping reduce developmental periods. None of the E-stim double bar classes with stimulus motion in directions D1 and D2 were classified according to heir L-stim induced training measurements of reference. This is likely caused by the fact that the stimuli moving in these directions were presented in different activation patterns of the electrodes, as limited by the MEA layout (see figure 2.2). Compared to E-stim electrode activation with directions D3 and D4, the more sparse activation of E-stim in directions D1 and D2 therefore seem to not sufficiently satisfy a required stimulation input to achieve according response patterns. This means that if one would expect an equally good classification accuracy of responses to double bar stimuli moving in all four directions (D1-D4), the MEA layout should be of a different kind. Another option would be the adaptation of the stimuli moving in directions D1 and D2, to satisfy the expected responses, if possible.

As the fact of an almost uniform spacing of cells across the retina in a given mosaic (Roska, 2014) was useful in this approach, the focus of classification was to obtain input-output statements, regardless retinal tissue orientation (see chapter 4.1.2). Based on this, the approach can rather be considered an analysis of velocities and bar spacings without focusing on the directions of motion. This means that the classification quality of responses to motion in direction D3 can also be expected for D4 induced responses. Therefore D3 and D4 were used as mutual control measures and D1 and D2 as the same for each other.

As expected, it was possible to reduce the original test dataset with 24 E-stim induced response classes (figure 3.15 (A), Set 1), to a subset of most useful E-stim classes (figure 3.15 (A), Set 8). Based on these observations, useful bar spacings for double bar stimulation could be determind. Considering the spatial resolution and layout of the MEA, this approach gives hints about the redundancy in terms of how much of an object structure is required so that E-stim induced responses can approximate L-stim induced responses to a useful degree. To optimize the subset obtained from this evaluation, further iterations involving further stimulus variations would be required. Although this sort of stimulus optimization was not part of this study, such iterations could also include E-stim tests with bar spacings in between the here shown 40 μm and 240 μm for moving stimuli. Another interesting aspect regarding spatial redundancy is the relatively large electrode size used in retinal implants (Zrenner, 2002; Margalit, 2002; Yanai, 2007; Zrenner, 2010; Mathieson, 2012; Humayun, 2012; Zrenner, 2013; Saunders, 2013; Ayton, 2014; Stingl, 2015; Bloch, 2019). The used spatial MEA resolution has a higher density, which allowed finer adjustments for spatio-temporal stimulus composition.

As a final statement on the classification, E-stim single bars (D1 - D4) were classified correctly, and double bars with a bar spacing of 240 μm (D3 or D4), all at a moderate velocity of v = 220 $\mu m/s$. Although there is a more

sparse E-stim activation at a given stimulation timepoint for the single bars when using stimulus directions D1 or D2, this electrode arrangement was sufficient to correctly classify the desired stimuli. Reliable classification of double bar E-stim is possible when using the more dense representation which is given in D3 and D4, with bar spacing = 240 μm and v = 220 $\mu m/s$. This implies that an inter-electrode distance of 40 μm between neighbouring electrodes should be considered for such a stimulus, rather than the more sparse configuration with 80 μm as used with directions D1 and D2.

4.2.2 Light Stimulation Patterns for Reference Data

A crucial aspect is the choice of the L-stim induced responses used for training ANNs as reference models. The stimulus set in this work is composed of an artificial stimulation paradigm. It would not be a problem to use other stimulation paradigms for L-stim, such as natural scenes, which would indeed also be artificial in their composed stimulation form. Regardless the many possibilities of future implementations, fundamental proofs of different principles should rather be performed on controlled stimuli, featuring basic object-shapes which are easily representable by electrical implants, as demonstrated in the present work. The stimuli should also be in a physiologically plausible range, to obtain a solid reference for a basic understanding. This was the intention in this work. More complex stimuli can be used in a later stage. Especially the implementation of such electrical paradigms would create higher difficulties, as it can be estimated from this study. It should be stressed that such tests depend on the used retinal tissue samples to a great extent. A main rule for such testing purposes should be, that E-stim patterns should be designed to mimic L-stim induced RGC responses as a fundamental design guidance, to achieve a sensible basis for testing within reasonable efforts, when regarding time contraints.

4.2.3 Plausibility of the Data-Based Artificial Neural Network Assisted Testing Approach

In this work, CNNs were utilized to capture spatiotemporal information of RGC responses obtained from RGC MEA-recordings with an application based hands-on approach in mind. With a visual acuity in the mouse of 0.5 cyc/deg (Prusky, 2000), one could ask the question, how ANN models correlate with the mouse visual apparatus: Maybe an ANN can resolve more cycles per degree and therefore outperform the natural condition of a mouse? How do future ANN models hold good for such a task? In the presented approach this was taken into account based on the fact that the ANNs learned exclusively from the retinal output, based on (physiologically) plausible stimuli as input. It also should be mentioned that the ambition was not to employ an approach with biologically inspired, nature-replicated RGC processing models on a detailed computational basis, but to assess E-stim induced RGC responses based on L-stim induced RGC responses to support developments aiding patients.

In the used approach, the ANNs are used for the input-output relationship with the retina being considered as a black box sensor. The ANNs do therefore not reveal detailed insights of biologically correct mechanisms. To this end, the approach was based on a pattern recognition problem with preceding experimental procedures and data processing. It could be shown, that employing CNNs with one convolutional layer sufficiently served a robust testing environment when using temporally binned RGC information in the form of binary inputs from multiple MEA-electrodes.

The results of the approach presented here imply that in complex computational works, CNNs do not necessarily have to have a deep architecture, which of course strongly depends on the problem to be solved. Using CNNs, features learned during training can not only give valuable insights for the tuning of

network parameters, but also for the composition of data used for training and testing, driving the iterative process.

Indeed, robustness and practicalness were keystones which were continuously followed in this work. The underlying concept of this data driven approach allowed an unrestricted design of the whole framework. A great advantage was the fact that the required tasks could be performed directly at first hand. This covers methodological planning over data acquisition and the development of algorithms to the final classifications. In general, the quality of the used data of course has an influence on the results. Although the test environment is in-vitro, when building a dataset, many measurements obtained from different tissue samples should yield a balanced dataset, subsequently influencing the models. This was taken care of during the experiments. The employed CNN architecture which was found to yield good results for the given problem could also be changed in future, replaced respectively. More experiments could be performed, further increasing and varying train/test set configurations for ANN-experiments.

In this work, data obtained from retinal tissues from healthy mouse retinas was used. The whole mouse retina can be compared to primate peripheral vision, because mice do not have a fovea (Krishnamoorthy, 2012). There is an almost uniform spacing of cells and cell type distribution across the retina in a given mosaic (Roska and Meister, 2014). In this work, the independency of retinal location and eccentricity for RGC recordings (Krishnamoorthy, 2012) was therefore a great advantage in the performed MEA-experiments: Retinal tissue orientation on the MEA was neglectable and was therefore arbitrary. Stimulus directions D1+D2 and D3+D4 served as mutual control measures regarding MEA-electrode arrangement (electrode arrangement D1 = D2, D3 = D4).

4.2.4 Modifications & Extensions of the Framework

The method can be applied for other stimulation paradigms as well: With other retinal tissues, MEAs, retinal implants or testing environments in general, always under the consideration of the respective sensible stimulation inputs. A next possible study could make use of E-stim induced responses obtained from diseased retinal tissues, to be used as test measurements with ANNs trained with the responses obtained from healthy retinal tissues.

Further, other processing paradigms and ANN architectures could also be used. For example using responses in the form of movie-sequences as input, if one is interested in feature representations of biologically inspired computations. With another research focus, approaches as described in Maheswaranathan (2018) were used to obtain insights on computational mechanisms of the retina. In any ANN based method, training data has an influence on the possible outcome. Regardless additional methods, extensions or optimizations of the presented approach, it should be stressed that the basic underlying problem will remain the same: The approximation of E-stim induced responses to L-stim induced responses. Although the tested method yields good results to get an estimate on how the tested E-stim patterns comply the L-stim patterns, it is likely that more data would lead to more accurate results, which is known for ANN based works. This approach could also be used in combination with other tools. For example approaches such as in Shah (2018) or Golden (2019) could be used as an additional source of information. A suitable test environment always depends on the requirements and the desired outcome. Regarding vision based on retinal responses, the shown approach could be repeated with retinal tissues from other species.

In the present study, data was obtained from healthy retinal tissue samples. A next step for testing E-stim induced RGC response patterns based on the

framework introduced in this work, could be performed with E-stim of retinal tissue samples from degenerative models of retinitis pigmentosa. In (Haq, 2017, 2018), where mouse retinas from rd1 mouse models were used, an implantation of subretinal implants at an early stage of retinitis pigmentosa was suggested. Considering the rewiring of circuitry in retinitis pigmentosa (Haq, 2014), an evaluation of E-stim induced RGC responses at different stages of retinal degeneration would make sense. Therefore it is suggested, to apply E-stim patterns used in this work to mouse retinal tissues with degenerative features. Then the same testing principle as shown in this thesis could be used to compare those E-stim induced RGC responses by employing ANNs trained on L-stim induced RGC response data obtained from healthy retinal tissues. Even when considering the testing of E-stim strategies with retinal explants taken from animals or even artificial cultures, such a framework could be used as an indirect measure in the form of a more or less sophisticated look up table based on the ANN outputs, to build relations to human vision. Also, established E-stim strategies could be re-assessed under other conditions, such as in drug tests. Another perspective is the use of such an ANN based approach for applications making use of an online feedback, possibly also working as an implementation based on embedded systems.

4.2.5 Implications for the Development of Electrical Retinal Implants

Numerous new developments of electrode materials and possible stimulation strategies are being tested in computational, laboratory and clinical environments to improve vision with the help of retinal implants. However, final performance of applied E-stim patterns can be only assessed in clinical trials with direct feedback from patients. Also as an indirect measure for retinal implant research, this tool set can be employed for comparative analyses, when used to assess in-vitro laboratory data such as comparing electrode materials for the development of small and super-conductive electrodes, new MEAs, behaviour with retinal tissues

from other species or new retinal implants.

The robustness of the approach comes with the fact that the final output is not a constructed stimulus or a final recommendation for E-stim, but an estimate for the exclusion of stimuli that will likely not work, and for the ones that work, considering the used test environment and the conditions. Based on such results, new stimuli can then be implemented and tested again with the appropriate L-stim induced RGC response based reference. Stimuli for E-stim can vary in strenth, pulse duration and shape-type (square, triangular, sinewave, ...). This means that, when trying to optimize or refine a particular stimulation strategy, the required efforts for stimulus design, data acquisition and testing could increase drastically, depending on the needs and the task. On the other hand one can break down the approach if the task allows this, using smaller datasets to obtain rough estimates. The discussed testing framework yields a first practical use of its kind for the support in designing E-stim patterns, testing new developments respectively.

The shown results from the methods to counteract fading effects are an application that can be supported through the introduced testing framework. These positive results also show that the design of E-stim patterns supported through the ANN testing framework does not necessarily need to be based on detailed numbers exclusively. Obtaining estimates based on the introduced testing framework can therefore yield valuable orientations for the construction of E-stim patterns used in electrical retinal implants. In a further stage, the testing approach could also be used for in-vitro tests with retinal implants or equivalent tools for pre-clinical tests. This way, the implant would be activated through L-stim, and the respective E-stim could be tested based on the RGC recordings. To summarize, the here introduced testing framework could help shorten engineering loops on the basis of a combined set of methods for the early assessment of E-stim patterns for electrical retinal implants in pre-clinical tests.

4.3 Conclusion

This tool set aids the evaluation and approximation of E-stim induced RGC responses to L-stim induced responses. This allows a functional benchmarking of new electrical stimulation patterns and novel implant chip designs already before implementing them into actual implants followed by the testing phase with affected patients. The introduced methods build a framework for the testing and the creation of efficient electrical stimulation paradigms. The approach presented here can be used in combination with other tools, to gain a broad perspective on the respective stimulation paradigm of interest. This framework can be understood as a set of tools, in the shown case based on data from healthy mouse retinal explants as a proof of principle.

5 Summary

Electrical stimulation (E-stim) of the retina with electrode arrays can be employed to evoke visual sensations for patients blinded by photoreceptor dystrophy due to retinitis pigmentosa. Although E-stim through electrical retinal implants (E-retinal-implants) can provide benefits for affected patients in daily life, the temporal and spatial resolution of perceived visual sensations need to be optimized. A driving question is, if the perceived visual sensations in patients are an appropriate representation of the objects in their visual perception. To date, only patients can answer this question. In terms of developing E-retinal-implants to aid vision, this appears to be a very late stage in the development of implants for a qualified answer to this question. In this work, an experimental and analytical basic concept was developed, which allows to estimate the degree to which the retina has coded the desired object in terms of recognition. Regarding the minimal needs for object recognition by blind patients, a black-box approach is described on the meta-level, where all recorded retinal ganglion cell (RGC)-responses are considered. As a fundamental building block, an electrophysiological multielectrode array (MEA)-setup for recording both, light stimulation (L-stim) and E-stim induced RGC responses in epiretinal configuration from healthy mouse retinal explants was used. L-stim patterns were applied as single bars and as double bars with different bar spacings at different velocities in four directions. With this, a library consisting of L-stim induced RGC responses with 104 classes was created. E-stim patterns were presented analogously through the MEA electrodes. Since this approach includes complex stimulus and response constellations, artificial neural networks (ANNs) for pattern recognition were applied to detect E-stim induced objects. As a robust ANN architecture, convolutional ANNs were employed. To test and assess the approximation quality of E-stim, E-stim induced response sequences were presented to the ANNs trained with L-stim induced classes. Six E-stim classes were correctly classified with approximately 96 % accuracy by the networks which were exclusively trained with the 104-class library from light evoked responses. For different object structures, this approach can give hints about redundant components in the stimulus structure. Through this, it can be estimated to which degree a certain object structure is required so that L-stim induced responses can be approximated by E-stim induced responses to a useful degree. The here developed set of analysis-tools supports the evaluation and approximation of E-stim induced RGC responses to L-stim induced responses. This allows an assessment of the functionality of new E-stim patterns already before implementing respective solutions in E-retinal-implants and ahead of the testing phase with affected patients. It was possible to reduce the original test dataset with 24 E-stim induced classes to a subset of most useful classes. With the help of such an approach, new E-stim strategies could already be narrowed down to a limited parameter space, which in turn could help shorten future design procedures of retinal implants.

6 Zusammenfassung

Elektrostimulation (E-stim) der Retina mit Elektrodenfeldern kann eingesetzt werden, um Seheindrücke für blinde Patienten hervorzurufen, die an Photorezeptor Dystrophie durch Retinitis Pigmentosa erblindet sind. Obwohl es möglich ist, mit E-stim durch elektrische Retina-Implantate (E-Retina-Implantate) betroffenen Patienten im täglichen Leben Seheindrücke zu ermöglichen, bedarf die zeitliche und räumliche Auflösung der visuellen Wahrnehmung einer Optimierung. Eine wichtige Frage ist, ob die Seheindrücke eine angemessene Repräsentation der Objekte in der visuellen Perzeption der Patienten darstellen. Bisher können nur Patienten diese Frage beantworten. In der Kette der Implantatentwicklung erscheint dies jedoch als ein sehr später Zeitpunkt für eine qualifizierte Antwort auf diese Frage. In dieser Arbeit wurde deshalb ein experimentelles und analytisches Grundkonzept entwickelt, das es erlaubt, einzuschätzen, bis zu welchem Grad die Retina das gewünschte Objekt erkennungsrelevant kodiert hat. Mit Blick auf die minimalen Bedürfnisse für Objekterkennung blinder Patienten wird ein Black-Box Ansatz auf Meta-Ebene beschrieben, in dem alle aufgezeichneten retinalen Ganglienzell (RGC)-Antworten berücksichtigt werden. Als ein Grundbaustein wurde ein elektrophysiologisches Multielektroden Array (MEA)-Setup eingesetzt, um Lichtstimulations- (L-stim) und E-stim induzierte retinale Ausgangssignale von gesunden Mausretina-Explantaten in epiretinaler Konfiguration aufzuzeichnen. L-stim Muster wurden durch Einzel-Balken und Doppel-Balken mit verschiedenen Balken-Abständen bei verschiedenen Geschwindigkeiten in vier Richtungen appliziert. Damit wurde eine Bibliothek aus L-stim induzierten RGC-Antworten mit 104 Klassen erstellt. E-stim Muster wurden in analoger Weise durch entsprechende Ansteuerung der MEA-Elektroden präsentiert. Da der Ansatz komplexe Reiz und Antwort Konstellationen beinhaltet, wurden künstliche neuronale Netze (engl. artificial neural networks, ANNs) verwendet, um E-stim induzierte Objekte korrekt zu klassifizieren. Als robuste ANN-Architektur wurden Faltungsnetze (engl. convolutional neural networks, CNNs) verwendet. Im Anschluss an das Training mit den L-stim induzierten Klassen, wurden E-stim induzierte Antwort-Sequenzen den ANNs zugeführt, um die E-stim-Annäherungsqualität zu testen und zu beurteilen. Sechs E-stim Klassen wurden mit circa 96 % Genauigkeit korrekt anhand der Netzwerke klassifiziert, die ausschließlich mit der 104-Klassen Bibliothek von Licht-evozierten Antworten trainiert wurden. Für verschiedene Objektstrukturen kann dieser Ansatz Hinweise auf redundante Anteile in der Stimulusstruktur geben. Hierdurch kann abgeschätzt werden, in welchem Ausmaß eine Objektstruktur benötigt wird, um L-stim induzierte Antworten durch E-stim induzierte Antworten in einem nützlichen Umfang annähern zu können. Der hier entwickelte Satz an Analysewerkzeugen unterstützt die Evaluierung und Annäherung E-stim induzierter RGC Antworten an L-stim induzierte Antworten. Dies erlaubt eine Beurteilung der Funktionalität neuer E-stim Muster bereits vor der Implementierung entsprechender Lösungen in E-Retina-Implantaten vor der Testphase mit betroffenen Patienten. Der ursprüngliche Test-Datensatz mit 24 E-stim induzierten Klassen konnte auf eine Teilmenge mit den nützlichsten Klassen reduziert werden. Mit der Hilfe eines solchen Ansatzes könnten neue E-stim Strategien bereits auf einen begrenzten Parametersatz eingegrenzt werden. Dies kann künftige Entwurfsprozesse von Retina-Implantaten zeitlich deutlich verkürzen.

7 Abbreviations

AC	Amacrine Cell
ANN	Artificial Neural Network
BC	Bipolar Cell
$BSpace$	Bar Spacing
CNN	Convolutional Neural Network
DSI	Direction Selective Index
$E-stim$	Electrical stimulation
ERL	Electrical stimulation induced Response Library
HC	Horizontal Cell
HL	Hidden Layer
$L-stim$	Light stimulation
LRL	Light stimulation induced Response Library
MCS	Multi Channel Systems MCS GmbH, Reutlingen, Germany
MEA	MultiElectrode Array
NR	Normalized number of Recording electrodes
PhR	PhotoReceptor
RGC	Retinal Ganglion Cell
TMW	The MathWorks, Inc., Natick, MA, USA

8 Bibliography

Ayton LN, Blamey PJ, Guymer RH, et al. (2014). First-in-Human Trial of a Novel Suprachoroidal Retinal Prosthesis. PLoS One 9, e115239.

Badea TC, Nathans J (2004). Quantitative analysis of neuronal morphologies in the mouse retina visualized by using a genetically directed reporter. The Journal of Comparative Neurology 480, 331-351.

Baden T, Berens P, Franke K, Román Rosón M, Bethge M, Euler T (2016). The functional diversity of retinal ganglion cells in the mouse. Nature 529, 345-350.

Barlow HB, Hill RM (1963). Selective sensitivity to direction of movement in ganglion cells of the rabbit retina. Science 139, 412.

Basavaraju S, Speck A, Haq W, Zrenner E (2018). Presentation of human microsaccade patterns to the mouse retina: Understanding image fading by electrical stimulation. Meeting Abstract. New Horizons in Vision and Hearing Research, Tübingen, Germany.

Baylor DA, Fuortes MGF, O'Bryan PM (1971). Receptive fields of cones in the retina of the turtle. The Journal of Physiology 214, 265-294.

Behrend MR, Ahuja AK, Humayun MS, Chow RH, Weiland JD (2011). Resolution of the Epiretinal Prosthesis is not Limited by Electrode Size. IEEE Transactions on Neural Systems and Rehabilitation Engineering 19, 436-442.

Berry MJ II, Brivanlou IH, Jordan TA, Meister M (1999). Anticipation of moving stimuli by the retina. Nature 398, 334-338.

Bishop CM (2006). Pattern Recognition and Machine Learning. Springer Science+Business Media.

Bleckert A, Schwartz GW, Turner MH, Rieke F & Wong ROL (2014). Visual space is represented by nonmatching topographies of distinct mouse retinal ganglion cell types. Current Biology 24, 310-315.

Bloch E, Luo Y, da Cruz L (2019). Advances in retinal prosthesis systems. Therapeutic Advances in Ophthalmology 11, 1-16.

Bloomfield SA, Völgyi B (2009). The diverse functional roles and regulation of neuronal gap junctions in the retina. Nature Reviews Neuroscience 10, 495-506.

Boinagrov D, Pangratz-Fuehrer S, Goetz G, Palanker D (2014). Selectivity of Direct and Network-mediated Stimulation of the Retinal Ganglion Cells with Epi-, Sub- and Intra-Retinal Electrodes. Journal of Neural Engineering 11.

Breuninger T (2010). Chromatic properties of bipolar cells in the mouse retina. Dissertation, Ruperto-Carola University of Heidelberg. DOI: 10.11588/heidok.00011553, URN: urn:nbn:de:bsz:16-opus-115533.

Briggman KL & Euler T (2011). Bulk electroporation and population calcium imaging in the adult mammalian retina. Journal of Neurophysiology 105, 2601-2609.

Bunker CH, Berson EL, Bromley WC, Hayes RP, Roderick TH (1984). Prevalence of Retinitis Pigmentosa in Maine. American Journal of Ophthalmology 97, 357-365.

Carcieri SM, Jacobs AL, Nirenberg S (2003). Classification of retinal ganglion cells: a statistical approach, Journal of Neurophysiology 90, 1704-1713.

Cepko C (2014). Intrinsically different retinal progenitor cells produce specific types of progeny. Nature Reviews Neuroscience 15, 615-627.

Chichilnisky EJ (2001). A simple white noise analysis of neuronal light responses. Network: Computation in Neural Systems 12, 199-213.

Coombs J, van der List D, Wang GY, Chalupa LM (2006). Morphological properties of mouse retinal ganglion cells. Neuroscience 140, 123-136.

Coombs JL, Van Der List D, Chalupa LM (2007). Morphological properties of mouse retinal ganglion cells during postnatal development. The Journal of Comparative Neurology 503, 803-814.

Curcio CA, Allen KA (1990). Topography of ganglion cells in human retina. The Journal of Comparative Neurology 300, 5-25.

Cybenko G (1989). Approximation by superpositions of a sigmoidal function. Mathematics of Control, Signals, and Systems 2, 303-314.

Dacey DM (1993). The mosaic of midget ganglion cells in the human retina. Journal of Neuroscience 13, 5334-5355.

Dacey DM, Peterson BB, Robinson FR, Gamlin PD (2003). Fireworks in the primate retina: in vitro photodynamics reveals diverse LGN-projecting ganglion cell types. Neuron 37, 15-27.

Demb JB, Singer JH (2015). Functional Circuitry of the Retina. Annual Review of Vision Science 1, 263-289.

Dräger UC, Olsen JF (1980). Origins of crossed and uncrossed retinal projections in pigmented and albino mice. The Journal of Comparative Neurology 191, 383-412.

Dräger UC, Olsen JF (1981). Ganglion cell distribution in the retina of the mouse. Investigative Ophthalmology & Visual Science 20, 285-293.

Ecker JL, Dumitrescu ON, Wong KY, Alam NM, Chen SK, LeGates T, Renna JM, Prusky GT, Berson DM, Hattar S (2010). Melanopsin-expressing retinal

ganglion-cell photoreceptors: cellular diversity and role in pattern vision. Neuron 67, 49-60.

Eckmiller R, Baruth O, Borbe S (2008). Towards Learning Retina Implants: How to Induce Visual Percepts with Electrical Stimulation Patterns. In: Wang R, Shen E, Gu F (eds) Advances in Cognitive Neurodynamics ICCN 2007. Springer, Dordrecht.

Elstrott J, Anishchenko A, Greschner M, Sher A, Litke AM, Chichilnisky EJ, Feller MB (2008). Direction Selectivity in the Retina Is Established Independent of Visual Experience and Cholinergic Retinal Waves. Neuron 58, 499-506.

Euler T, Detwiler PB, Denk W (2002). Directionally selective calcium signals in dendrites of starburst amacrine cells. Nature 418, 845-852.

Euler T, Baden T (2016). Computational neuroscience: Species-specific motion detectors. Nature 535, 45-46.

Farrow K, Masland RH (2011). Physiological clustering of visual channels in the mouse retina, Journal of Neurophysiology 105, 1516-1530.

Farrow K, Teixeira M, Szikra T, Viney TJ, Balint K, Yonehara K, Roska B (2013). Ambient illumination toggles a neuronal circuit switch in the retina and visual perception at cone threshold. Neuron 78, 325-338.

Field GD, Greschner M, Gauthier JL, Rangel C, Shlens J, Sher A, Marshak DW, Litke AM, Chichilnisky EJ (2009). High-sensitivity rod photoreceptor input to the blue-yellow color opponent pathway in macaque retina. Nature Neuroscience 12, 1159-1164.

Fiscella M, Farrow K, Jones IL, Jäckel D, Müller J, Frey U, Bakkum DJ, Hantz P, Roska B, Hierlemann A (2012). Recording from defined populations of retinal ganglion cells using a high-density CMOS-integrated microelectrode array with real-time switchable electrode selection. Journal of Neuroscience Methods 211, 103-113.

Fornos AP, Sommerhalder J, da Cruz L, Sahel JA, Mohand-Said S, Hafezi F, Pelizzone M (2012). Temporal Properties of Visual Perception on Electrical Stimulation of the Retina. Investigative Ophthalmology & Visual Science 53, 2720-2731.

Freeman DK, Fried SI (2011). Multiple Components of Ganglion Cell Desensitization in Response to Prosthetic Stimulation. Journal of Neural Engineering 8.

Fried SI, Münch TA, Werblin FS (2002). Mechanisms and circuitry underlying directional selectivity in the retina. Nature 420, 411-414.

Golden JR, Erickson-Davis C, Cottaris NP, Parthasarathy N, Rieke F, Brainard DH, Wandell BA, Chichilnisky EJ (2019). Simulation of visual perception and learning with a retinal prosthesis. Journal of Neural Engineering 16.

Gollisch T, Meister M (2010). Eye smarter than scientists believed: neural computations in circuits of the retina. Neuron 65, 150-164.

Hack I, Peichl L, Brandstätter JH (1999). An alternative pathway for rod signals in the rodent retina: rod photoreceptors, cone bipolar cells, and the localization of glutamate receptors. Proceedings of the National Academy of Sciences of the United States of America 96, 14130-14135.

Hafed ZM, Stingl K, Bartz-Schmidt KU, Gekeler F, Zrenner E (2016). Oculomotor behavior of blind patients seeing with a subretinal visual implant. Vision Research 118, 119-131.

Hamel C (2006). Retinitis pigmentosa. Orphanet Journal of Rare Diseases 1.

Haq W, Arango-Gonzalez B, Zrenner E, Euler T, Schubert T (2014). Synaptic remodeling generates synchronous oscillations in the degenerated outer mouse retina. Frontiers in Neural Circuits 8.

Haq W, Dietter J, Zrenner E (2018). Electrical activation of degenerated photoreceptors in blind mouse retina elicited network-mediated responses in different types of ganglion cells. Scientific Reports 8.

Haq W, Speck A, Basavaraju S, Dieter J, Zrenner E (2017). Electrically activated dormant photoreceptors elicit network-mediated responses in different types of ganglion cells. Meeting Abstract. Artificial Vision, Aachen, Germany. Düsseldorf: German Medical Science GMS Publishing House.

Hartline HK (1938). The response of single optic nerve fibers of the vertebrate eye to illumination of the retina. American Journal of Physiology 121, 400-415.

Hartong DT, Berson EL, Dryja TP (2006). Retinitis pigmentosa. The Lancet 368, 1795-1809.

Hattar S, Liao HW, Takao M, Berson DM, Yau KW (2002). Melanopsin-containing retinal ganglion cells: Architecture, projections, and intrinsic photosensitivity. Science 295, 1065-1070.

Hong YK, Kim IJ, Sanes JR (2011). Stereotyped axonal arbors of retinal ganglion cell subsets in the mouse superior colliculus. The Journal of Comparative Neurology 519, 1691-1711.

Huberman AD, Manu M, Koch SM, Susman MW, Lutz AB, Ullian EM, Baccus SA, Barres BA (2008). Architecture and activity-mediated refinement of axonal projections from a mosaic of genetically identified retinal ganglion cells. Neuron 59, 425-438.

Huberman AD, Wei W, Elstrott J, Stafford BK, Feller MB, Barres BA (2009). Genetic identification of an On-Off direction-selective retinal ganglion cell subtype reveals a layer-specific subcortical map of posterior motion. Neuron 62, 327-334.

Hughes S, Watson TS, Foster RG, Peirson SN, Hankins MW (2013). Nonuniform distribution and spectral tuning of photosensitive retinal ganglion cells of the mouse retina. Current Biology 23, 1696-1701.

Humayun MS, Dorn JD, da Cruz L, et al. (2012). Interim Results from the International Trial of Second Sight's Visual Prosthesis. Ophthalmology 119, 779-788.

Illing RB, Wässle H (1981). The retinal projection to the thalamus in the cat: A quantitative investigation and a comparison with the retinotectal pathway. The Journal of Comparative Neurology 202, 265-285.

Jeon CJ, Strettoi E, Masland RH (1998). The major cell populations of the mouse retina. Journal of Neuroscience 18, 8936-8946.

Jepson LH, Hottowy P, Weiner GA, Dabrowski W, Litke AM, Chichilnisky EJ (2014). High-fidelity reproduction of spatiotemporal visual signals for retinal prosthesis. Neuron 83, 87-92.

Johnson KP, Zhao L, Kerschensteiner D (2018). A Pixel-Encoder Retinal Ganglion Cell with Spatially Offset Excitatory and Inhibitory Receptive Fields. Cell Reports 22, 1462-1472.

Johnston J, Lagnado L (2015). General features of the retinal connectome determine the computation of motion anticipation. eLIFE 4, e06250.

Kay JN, De la Huerta I, Kim IJ, Zhang Y, Yamagata M, Chu MW, Meister M, Sanes JR (2011). Retinal ganglion cells with distinct directional preferences differ in molecular identity, structure, and central projections. Journal of Neuroscience 31, 7753-7762.

Kim IJ, Zhang Y, Yamagata M, Meister M, Sanes JR (2008). Molecular identification of a retinal cell type that responds to upward motion. Nature 452, 478-482.

Kim IJ, Zhang Y, Meister M, Sanes JR (2010). Laminar restriction of retinal ganglion cell dendrites and axons: subtype-specific developmental patterns revealed with transgenic markers. Journal of Neuroscience 30, 1452-1462.

Kolb H, Nelson R (1993). OFF-alpha and OFF-beta ganglion cells in cat retina: II. Neural circuitry as revealed by electron microscopy of HRP stains. The Journal of Comparative Neurology 329, 85-110.

Kolb H (1994). The architecture of functional neural circuits in the vertebrate retina. The Proctor Lecture. Investigative Ophthalmology % Visual Science 35, 2385-2404.

Kong JH, Fish DR, Rockhill RL, Masland RH (2005). Diversity of ganglion cells in the mouse retina: unsupervised morphological classification and its limits. The Journal of Comparative Neurology 489, 293-310.

Krishnamoorthy V (2012). Encoding of saccadic scene changes in the mouse retina. Dissertation, LMU München: Fakultät für Biologie. URN urn:nbn:de:bvb:19-150913.

Kuffler SW (1953). Discharge patterns and functional organization of mammalian retina. Journal of Neurophysiology 16, 37-68.

LeCun Y, Bengio Y, Hinton G (2015). Deep learning. Nature 521, 436-444.

Levick WR (1967). Receptive fields and trigger features of ganglion cells in the visual streak of the rabbits retina. The Journal of Physiology 188, 285-307.

Münch TA, da Silveira RA, Siegert S, Viney TJ, Awatramani GB, Roska B (2009). Approach sensitivity in the retina processed by a multifunctional neural circuit. Nature Neuroscience 12, 1308-1316.

Maheswaranathan N, McIntosh L, Kastner DB, Melander J, Brezovec L, Nayebi A, Wang J, Ganguli S, Baccus SA (2018). Deep learning models reveal internal structure and diverse computations in the retina under natural scenes. bioRxiv preprint, not peer-reviewed. DOI: https://doi.org 10.1101/340943; History Version: June 14, 2018.

Margalit E, Maia M, Weiland JD, et al. (2002). Retinal Prosthesis for the Blind. Survey of Ophthalmology 47, 335-356.

Marre O, Botella-Soler V, Simmons KD, Mora T, Tkačik G, Berry MJ II (2015). High Accuracy Decoding of Dynamical Motion from a Large Retinal Population. PLoS Computational Biology 11, e1004304.

Martinez-Conde S, Macknik SL, Hubel DH (2004). The role of fixational eye movements in visual perception, Nature Reviews Neuroscience 5, 229-40.

Masland RH (2001). The fundamental plan of the retina. Nature Neuroscience 4, 877-886.

Masland RH (2011). Cell populations of the retina: the Proctor lecture. Investigative Ophthalmology % Visual Science 52, 4581-4591.

Masland RH (2012). The neuronal organization of the retina. Neuron 76, 266-280.

Mathieson K, Loudin J, Goetz G, et al. (2012). Photovoltaic retinal prosthesis with high pixel density. Nature Photonics 6, 391-397.

Matteucci PB, Barriga-Rivera A, Eiber CD, Lovell NH, Morley JW, Suaning GJ (2016). The Effect of Electric Cross-Talk in Retinal Neurostimulation. Investigative Ophthalmology & Visual Science 57, 1031-1037.

Mazurek M, Kager M, Van Hooser SD (2014). Robust quantification of orientation selectivity and direction selectivity. Frontiers in Neural Circuits 8.

McIntosh LT, Maheswaranathan N, Nayebi A, Ganguli S, Baccus SA (2016). Deep Learning Models of the Retinal Response to Natural Scenes. Conference Paper. 30th Conference on Neural Information Processing Systems, Barcelona, Spain. In: Advances in Neural Information Processing Systems 29, Curran Associates Inc., 1369-1377.

Møller MF (1993). A Scaled Conjugate Gradient Algorithm for Fast Supervised Learning. Neural Networks 6, 525-533.

Naarendorp F, Esdaille TM, Banden SM, Andrews-Labenski J, Gross OP, Pugh EN Jr. (2010). Dark light, rod saturation, and the absolute and incremental sensitivity of mouse cone vision. Journal of Neuroscience 30, 12495-12507.

Nelson R, Kolb H, Freed MA (1993) OFF-alpha and OFF-beta ganglion cells in cat retina. I: Intracellular electrophysiology and HRP stains. The Journal of Comparative Neurology 329, 68-84.

Ölveczky BP, Baccus SA, Meister M (2003). Segregation of object and background motion in the retina. Nature 423, 401-408.

Parthasarathy N, Batty E, Falcon W, Rutten T, Rajpal M, Chichilnisky EJ, Paninski L (2017). Neural Networks for Efficient Bayesian Decoding of Natural Images from Retinal Neurons. Conference Paper. 31st Conference on Neural Information Processing Systems, Long Beach, CA, USA. In: Advances in Neural Information Processing Systems 30, Curran Associates Inc., 6434-6445.

Pillow JW, Shlens J, Paninski L, Sher A, Litke AM, Chichilnisky EJ, Simoncelli EP (2008). Spatio-temporal correlations and visual signalling in a complete neuronal population. Nature 454, 995-999.

Prusky GT, West PWR, Douglas RM (2000). Behavioral assessment of visual acuity in mice and rats. Vision Research 40, 2201-2209.

Puchalla JL, Schneidman E, Harris RA, Berry MJ (2005). Redundancy in the Population Code of the Retina. Neuron 46, 493-504.

Ramón y Cajal S (1892). La rétine des vertébrés. La Cellule 1, 119-257 , Translation: Thorpe SA, Glickstein M (1972). Introduction to: The Structure of the Retina. Springfield (IL). C.C. Thomas.

Remtulla S, Hallett P (1985). A schematic eye for the mouse, and comparisons with the rat. Vision Research 25, 21-31.

Rodieck RW (1998). The First Steps in Seeing, Sinauer Associates Inc. Sunderland, MA.

Roska B, Meister M (2014). The Retina Dissects the Visual Scene into Distinct Features. Ed. Werner JS and Chalupa LM. The New Visual Neurosciences, MIT Press, Cambridge, MA, USA.

Russel WMS, Burch RL (1959). The principles of humane experimental technique. Methuen, London, UK.

Ryu SB, Ye JH, Lee JS, Goo YS, Kim CH, Kim KH (2009). Electrically-evoked Neural Activities of rd1 Mice Retinal Ganglion Cells by Repetitive Pulse Stimulation. The Korean Journal of Physiology & Pharmacology 13, 443-448.

Saunders AL, Williams CE, Heriot W, et al. (2013). Development of a surgical procedure for implantation of a prototype suprachoroidal retinal prosthesis. Clinical and Experimental Ophthalmology 42, 665-674.

Schaeffel F (2017). Sehleistungen von Tieren und Menschen im Vergleich. Der Ophthalmologe 114, 976-977.

Schaeffel F (2017). Vergleichende Betrachtung von Lichtempfindlichkeit, Tiefenwahrnehmung und Bewegungswahrnehmung bei Tier und Mensch. Der Ophthalmologe 114, 997-1007.

Schubert T, Maxeiner S, Krüger O, Willecke K, Weiler R (2005). Connexin45 mediates gap junctional coupling of bistratified ganglion cells in the mouse retina. The Journal of Comparative Neurology 490, 29-39.

Sekhar S, Jalligampala A, Zrenner E, Rathbun DL (2017). Correspondence between visual and electrical input filters of ON and OFF mouse retinal ganglion cells. The Journal of Neural Engineering 14.

Shah NP, Madugula S, Chichilnisky EJ, Singer Y, Shlens J (2018). Learning a neural response metric for retinal prosthesis. Conference Paper. Sixth International Conference on Learning Representations, Vancouver, BC, Canada.

Soucy E, Wang Y, Nirenberg S, Nathans J, Meister M (1998). A novel signaling pathway from rod photoreceptors to ganglion cells in mammalian retina. Neuron 21, 481-493.

Spear PD, Kim CBY, Ahmad A, Tom BW (1996). Relationship between numbers of retinal ganglion cells and lateral geniculate neurons in the rhesus monkey. Visual Neuroscience 13, 199-203.

Speck A, Basavaraju S, Haq W, Zrenner E (2018). Motion detection in retinal ganglion cell spikes through pattern recognition with a shallow artificial neural network. Meeting Abstract. New Horizons in Vision and Hearing Research, Tübingen, Germany.

Stett A, Barth W, Weiss S, Haemmerle H, Zrenner E (2000). Electrical multisite stimulation of the isolated chicken retina. Vision Research 40, 1785-1795.

Stett A, Mai A, Herrmann T (2007). Retinal charge sensitivity and spatial discrimination obtainable by subretinal implants: key lessons learned from isolated chicken retina. Journal of Neural Engineering 4, 7-16.

Stingl K, Bartz-Schmidt KU, Besch D, et al. (2013). Artificial vision with wirelessly powered subretinal electronic implant alpha-IMS. Proceedings of the Royal Society B 280, 20130077.

Stingl K, Schippert R, Bartz-Schmidt KU, et al. (2017). Interim Results of a Multicenter Trial with the New Electronic Subretinal Implant Alpha AMS in 15 Patients Blind from Inherited Retinal Degenerations. Frontiers in Neuroscience 11.

Stingl K, Bartz-Schmidt KU, Besch D, et al. (2015). Subretinal Visual Implant Alpha IMS - Clinical trial interim report. Vision Research 111, 149-160.

Stutzki H, Helmhold F, Eickenscheidt M, Zeck G (2016). Subretinal electrical stimulation reveals intact network activity in the blind mouse retina. Journal of Neurophysiology 116, 1684-1693.

Sun W, Li N, He S (2002). Large-scale morphological survey of mouse retinal ganglion cells. The Journal of Comparative Neurology 451, 115-126.

Szél Á, Röhlich P, Gaffé AR, Juliusson B, Aguirre G, Van Veen T (1992). Unique topographic separation of two spectral classes of cones in the mouse retina. The Journal of Comparative Neurology 325, 327-342.

Tanimoto N, Sothilingam V, Gloeckner G, Bryda EC, Humphries P, Biel M, Seeliger MW (2013). Auditory event-related signals in mouse ERG recordings. Documenta Ophthalmologica 128, 25-32.

Tortora GJ, Derrickson B (2009). Principles of anatomy and physiology, Twelfth Edition. John Wiley & Sons Inc.

Tsai TI, Joachimsthaler A, Kremers J (2017). Mesopic and Photopic Rod and Cone Photoreceptor-Driven Visual Processes in Mice With Long-Wavelength-Shifted Cone Pigments. Investigative Ophthalmology & Visual Science 58, 5177-5187.

Völgyi B, Chheda S, Bloomfield SA (2009). Tracer coupling patterns of the ganglion cell subtypes in the mouse retina. The Journal of Comparative Neurology 512, 664-687.

Wässle H, Grünert U, Röhrenbeck J, Boycott BB (1990). Retinal ganglion cell density and cortical magnification factor in the primate. Vision Research 30, 1897-1911.

Wang Z, Oates T (2015). Encoding Time Series as Images for Visual Inspection and Classification Using Tiled Convolutional Neural Networks. Conference Paper. Twenty-Ninth AAAI Conference on Artificial Intelligence. Trajectory-Based Behavior Analytics: Papers from the 2015 AAAI Workshop, Association for the Advancement of Artificial Intelligence, Austin, TX, USA.

Warland DK, Reinagel P, Meister M (1997). Decoding visual information from a population of retinal ganglion cells. Journal of Neurophysiology 78, 2336-2350.

Werblin FS (2010). Six different roles for crossover inhibition in the retina: correcting the nonlinearities of synaptic transmission. Visual Neuroscience 27, 1-8.

Wilke RGH, Moghadam GK, Lovell NH, Suaning GJ, Dokos S (2011). Electric crosstalk impairs spatial resolution of multi-electrode arrays in retinal implants. Journal of Neural Engineering 8.

Yanai D, Weiland JD, Mahadevappa M, Greenberg RJ, Fine I, Humayun MS (2007). Visual Performance using a retinal prosthesis in three subjects with retinitis pigmentosa. American Journal of Ophthalmology 143, 820-827.

Yonehara K, Shintani T, Suzuki R, Sakuta H, Takeuchi Y, Nakamura-Yonehara K, Noda M (2008). Expression of SPIG1 reveals development of a retinal ganglion cell subtype projecting to the medial terminal nucleus in the mouse. PLoS ONE 3, e1533.

Yoshida K, Watanabe D, Ishikane H, Tachibana M, Pastan I, Nakanishi S (2001). A key role of starburst amacrine cells in originating retinal directional selectivity and optokinetic eye movement. Neuron 30, 771-780.

Young T (1802). The Bakerian Lecture: On the theory of light and colours. Philosophical Transactions of the Royal Society London 92, 12-48.

Zhang Y, Kim IJ, Sanes JR, Meister M (2012). The most numerous ganglion cell type of the mouse retina is a selective feature detector. Proceedings of the National Academy of Sciences of the United States of America 109, E2391-E2398.

Zrenner E (2002). Will retinal implants restore vision?. Science 295, 1022-1025.

Zrenner E, Bartz-Schmidt KU, Benav H, et al. (2010). Subretinal electronic chips

allow blind patients to read letters and combine them to words. Proceedings of the Royal Society B 278, 1489-1497.

Zrenner E (2013). Fighting Blindness with Microelectronics. Science Translational Medicine 5, 210-216.

9 List of Figures

1.1 Schematic view of the sagittal section of the vertebrate eye and the retina . . . 2
1.2 Retinal implant approaches . . . 7
1.3 Schematic representation of the state-of-the-art procedure for retinal implant tests . . . 9
1.4 Schematic of the proposed procedure for testing new developments . 10
1.5 Proposed approach . . . 11

2.1 Schematic representation of the multielectrode recording setup . . . 14
2.2 Schematic representation of the light stimulation and electrical stimulation patterns . . . 17
2.3 Graphical user interface for light stimulation control . . . 18
2.4 Data processing for artificial neural network based classification. . . 23
2.5 Schematic of the underlying principle for pre-evaluation . . . 25
2.6 Schematic convolutional artificial neural network layout . . . 26

3.1 Responses to light flash stimulation . . . 30
3.2 Light stimulation induced retinal ganglion cell responses to single bars moving in directions D1-D4 . . . 33
3.3 Electrical stimulation induced retinal ganglion cell responses to single bars moving in directions D1-D4 . . . 34
3.4 Retinal ganglion cell response patterns in dependence on single bar and double bar stimulation . . . 36

3.5 Direction selective activity measured at single electrodes 37
3.6 Anticipation of motion to stimuli moving at v = 220 $\mu m/s$ 39
3.7 Anticipation of motion to stimuli moving at v = 550 $\mu m/s$ 40
3.8 Examples of light stimulation induced single measurements 42
3.9 Examples of electrically induced single measurements 43
3.10 Fraction of false classifications varying time bin size and number of neurons in the hidden layer 44
3.11 Convolutional neural network features 46
3.12 Example classification scheme 47
3.13 Classification of 24 electrically induced response classes 49
3.14 Classification of six electrically induced response classes 50
3.15 Constellations of different classes defined as Sets 51
3.16 Alternating electrical stimulation of double bars 54

10 Acknowledgements

I would like to thank Prof. Dr. med. Dr. h.c. mult. Eberhart Zrenner and Prof. Dr. Hanspeter Mallot for supervising my doctoral work. Further I thank Dr. Wadood Haq for the support as the immediate supervisor. I would like to thank Sunetra Basavaraju for the collaborative work and for the time through the doctoral work. Also, I would like to thank my family and friends. Thanks to Jayashree and Basavaraju. Greatest thanks I would like to express to my parents Kriemhilde and Peter Speck and my Brother Martin Speck. Further, I would like to thank the Tistou & Charlotte Kerstan Foundation for the project funding.